A Common Formalism for the Integral Formulations of the Forward EEG Problem

Jan Kybic, Maureen Clerc*, Toufic Abboud, Olivier Faugeras, Renaud Keriven, and Théo Papadopoulo

Abstract—The forward electroencephalography (EEG) problem involves finding a potential V from the Poisson equation $\nabla \cdot (\sigma \nabla V) = f$, in which f represents electrical sources in the brain, and σ the conductivity of the head tissues. In the piecewise constant conductivity head model, this can be accomplished by the boundary element method (BEM) using a suitable integral formulation. Most previous work uses the same integral formulation, corresponding to a double-layer potential. In this paper we present a conceptual framework based on a well-known theorem (Theorem 1) that characterizes harmonic functions defined on the complement of a bounded smooth surface. This theorem says that such harmonic functions are completely defined by their values and those of their normal derivatives on this surface. It allows us to cast the previous BEM approaches in a unified setting and to develop two new approaches corresponding to different ways of exploiting the same theorem. Specifically, we first present a dual approach which involves a single-layer potential. Then, we propose a symmetric formulation, which combines single- and double-layer potentials, and which is new to the field of EEG, although it has been applied to other problems in electromagnetism. The three methods have been evaluated numerically using a spherical geometry with known analytical solution, and the symmetric formulation achieves a significantly higher accuracy than the alternative methods. Additionally, we present results with realistically shaped meshes. Beside providing a better understanding of the foundations of BEM methods, our approach appears to lead also to more efficient algorithms.

Index Terms—Boundary element method, EEG, integral method, Poisson equation.

I. INTRODUCTION

ELECTROENCEPHALOGRAPHY (EEG) [1] is a non-invasive method of measuring the electrical activity of the brain. To reconstruct the sources in the brain (the inverse problem), an accurate forward model of the head must be established first. The so called *forward problem* addresses the
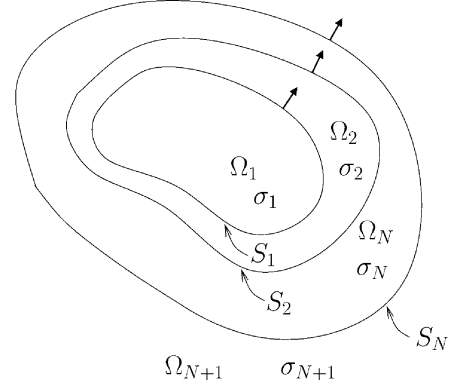
J. Kybic was with the Odyssée Laboratory – ENPC/ENS/INRIA BP93, 06902 Sophia-Antipolis, France. He is currently with the Center for Applied Cybernetics, Faculty of Electrical Engineering, Czech Technical University, Prague, Czech Republic (e-mail: kybic@fel.cvut.cz).

*M. Clerc is with the Odyssée Laboratory – ENPC/ENS/INRIA, 2004 Route des Lucioles, BP93, 06902 Sophia-Antipolis, France (e-mail: Maureen. Clerc@sophia.inria.fr).

T. Abboud is with the Applied Mathematics Center, Ecole Polytechnique, 91128 Palaiseau, France.

O. Faugeras, R. Keriven and T. Papadopoulo are with the Odyssée Laboratory ENPC/ENS/INRIA, 06902 Sophia-Antipolis, France.

Digital Object Identifier 10.1109/TMI.2004.837363

Fig. 1. The head is modeled as a set of nested regions $\Omega_1, \ldots, \Omega_{N+1}$ with constant conductivities $\sigma_1, \ldots, \sigma_{N+1}$, separated by interfaces $S_1, \ldots, S_N$. Arrows indicate the normal directions (outward).

calculation of the electric potential V on the scalp for a known configuration of the sources, provided that the physical properties of the head tissues (conductivities) are known. Note that the same forward model can be used for magnetoencephalography (MEG) [2], [3], since the magnetic field $\mathbf{B}$ can be calculated from the potential V by simple integration [4].

A. Problem Definition

The quasi-static approximation of Maxwell equations [2], [5] in a conducting environment yields the fundamental Poisson equation

$$\nabla \cdot \left(\sigma \nabla V \right) = f = \nabla \cdot \mathbf{J}^{\mathrm{P}} \quad \text{in } \mathbb{R}^3 \tag{1}$$

where $\sigma \, [(\Omega \cdot \mathrm{m})^{-1}]$ is the conductivity and f is the divergence of the current source density $\mathbf{J}^{\mathrm{P}} \, [\mathrm{A/m^2}]$, both supposed known in the forward problem; V (in volts) is the unknown electric potential.

We shall concentrate on a head model with piecewise-constant conductivity, such as shown in Fig. 1, with connected open sets Ω_i, separated by surfaces S_j. Note that for the sake of notational simplicity, in this paper we only consider nested regions with interfaces $S_i = \partial\Omega_i \cap \partial\Omega_{i+1}$. However, extension to other topologies is possible and straightforward.

The outermost volume Ω_{N+1} extends to infinity and in the EEG problem treated here the corresponding conductivity σ_{N+1} (the conductivity of air) is considered to be 0. This implies that there can be no source in Ω_{N+1}. We also assume that there are no charges there. The extension to $\sigma_{N+1} \neq 0$ is trivial.

B. Notation

We use the notation $\partial_{\mathbf{n}} V = \mathbf{n} \cdot \nabla V$ to denote the partial derivative of V in the direction of a unit vector $\mathbf{n}$, normal to an

interface S_j, $j = 1, \ldots, N$. A function f considered on the interface S_j will be denoted f_{S_j}. We define the jump of a function $f : \mathbb{R}^3 \to \mathbb{R}$ at interface S_j as

$$[f]_j = f_{S_j}^- - f_{S_j}^+$$

the functions f^- and f^+ on S_j being, respectively, the interior and exterior limits of f

$$\text{for } \mathbf{r} \in S_j, \qquad f_{S_j}^{\pm}(\mathbf{r}) = \lim_{\alpha \to 0^{\pm}} f(\mathbf{r} + \alpha \mathbf{n}).$$

Note that these quantities depend on the orientation of $\mathbf{n}$, which is taken outward by default, as shown in Fig. 1.

C. Connected Poisson Problems

Since the conductivity is supposed to be piecewise constant, we can factor out σ from (1) to yield a set of Poisson problems coupled by boundary conditions

$$\sigma_i \Delta V = f \quad \text{in } \Omega_i, \text{ for all } i = 1, \ldots, N \quad (2)$$
$$\Delta V = 0 \quad \text{in } \Omega_{N+1} \quad (3)$$
$$[V]_j = [\sigma \partial_{\mathbf{n}} V]_j = 0 \quad \text{on } S_j, \text{ for all } j = 1, \ldots, N. \quad (4)$$

Equation (3) is a Laplace equation arising from the fact that the conductivity is assumed to be zero and no charges present outside the head. Physically, the boundary condition $[V]_j = 0$ imposes the continuity of the potential across the interfaces. The quasi-static assumption implies the continuity of the current (charge) flow across the interfaces, which is expressed by the second boundary condition $[\sigma \partial_{\mathbf{n}} V]_j = 0$, as $\sigma \partial_{\mathbf{n}} V = \mathbf{n} \cdot \sigma E$ is precisely the density of current. Mathematically, both boundary conditions come from considering (1) on the boundaries.

D. Boundary Element Method (BEM)

The BEM [6], [7] is today a classical way of solving the forward problem. The advantage of the BEM with respect to the finite difference method (FDM) or the finite element method (FEM) resides in the fact that it only uses as unknowns the values on the interfaces between regions with different conductivities, as opposed to considering values everywhere in the volume. This reduces the dimensionality of the problem and the number of unknowns, and only requires the use of surface triangulation meshes, avoiding the difficult construction of the volume discretization needed for the FEM.

E. Inaccuracy of BEM Implementations

So far, the main disadvantage of using BEM in the EEG forward problem has been that in all known implementations the precision drops unacceptably when the distance d of the source to one of the surfaces becomes comparable to the size h of the triangles in the mesh (see also Section V-B1). This seriously hinders the usefulness of the BEM, as the sources which are measured by EEG are often supposed to lie in the cortex, which is only a few millimeters thick. Although the problem is widely acknowledged [8]–[11], no satisfactory solution has been found so far. Replacing the collocation by the Galerkin method [8], [12] for the resolution of the integral equations improves the precision only partially. The problem has largely been disregarded,

or sometimes avoided at the expense of excessively simplifying the model: some authors propose to omit either the outer cortex boundary, or the skull, claiming that these simplifications are inconsequential for the localization accuracy [13], [14]. Unfortunately, our experiments do not support this claim and there is direct and indirect evidence [15], [16] to show that accurate models are essential for accurate reconstruction. Note, however, that the MEG reconstruction is reportedly less affected by modeling errors than the EEG.

F. Proposed New Integral Formulation

As far as we know, all variants of the BEM applied to the EEG forward problem are based on the same integral formulation, introduced by Geselowitz [17] in 1967. However, this integral formulation is by no means the only one available. We show that the classical formulation corresponds to a double-layer potential approach. We propose a dual formulation using a single-layer potential. Finally, we present a new formulation, combining single- and double-layer potentials. This new approach leads to a symmetric system and turns out to be numerically significantly more accurate than the other two formulations.

G. Existing Work

There is a large body of literature describing BEM implementations using the double-layer potential formulation for forward and inverse EEG problems [8], [12], [18]–[22].

The symmetric formulation has existed in the BEM community for some time [7], [23]–[25], and the single-layer potential formulation has been used for solving elasticity problems [6], [7]. However, to the best of our knowledge, neither the symmetric approach nor the single-layer formulation have so far been applied to the EEG problem.

H. Organization of This Paper

We start in Section II by presenting the mathematical results needed for the BEM. Section III presents the classical double-layer potential formulation together with its dual formulation in terms of a single-layer potential, and the new symmetric integral formulation, which combines single- and double-layer potentials. The discretization and implementation are described in Section IV, followed by experimental results in Section V. Technical justifications and remarks relative to Section II are detailed in Appendix A and can be skipped at first reading.

II. REPRESENTATION THEOREM

The power of the BEM is in its conciseness, since it only requires to solve for values defined on surfaces instead of values defined in the volume. The key to this dimension reduction resides in a fundamental representation theorem [6], [7], which we recall in this section.

We define a Green function

$$G(\mathbf{r}) = \frac{1}{4\pi \|\mathbf{r}\|}$$

satisfying

$$-\Delta G = \delta_0. \quad (5)$$

Given a regular boundary (surface) $\partial\Omega$, we introduce four integral operators $\mathcal{D}, \mathcal{S}, \mathcal{N}, \mathcal{D}^*$, which map a scalar function f on $\partial\Omega$ to another scalar function on $\partial\Omega$

$$(\mathcal{D}f)(\mathbf{r}) = \int_{\partial\Omega} \partial_{\mathbf{n}'} G(\mathbf{r} - \mathbf{r}') f(\mathbf{r}') \, ds(\mathbf{r}')$$

$$(\mathcal{S}f)(\mathbf{r}) = \int_{\partial\Omega} G(\mathbf{r} - \mathbf{r}') f(\mathbf{r}') \, ds(\mathbf{r}')$$

$$(\mathcal{N}f)(\mathbf{r}) = \int_{\partial\Omega} \partial_{\mathbf{n},\mathbf{n}'} G(\mathbf{r} - \mathbf{r}') f(\mathbf{r}') \, ds(\mathbf{r}')$$

$$(\mathcal{D}^*f)(\mathbf{r}) = \int_{\partial\Omega} \partial_{\mathbf{n}} G(\mathbf{r} - \mathbf{r}') f(\mathbf{r}') \, ds(\mathbf{r}'). \qquad (6)$$

where $\mathbf{n}$, respectively, $\mathbf{n}'$, is the outward normal vector at position $\mathbf{r}$, respectively, $\mathbf{r}'$. Note that the operator $\mathcal{D}^*$ is the transpose (adjoint) of $\mathcal{D}$ with respect to the $L^2(\partial\Omega)$ scalar product $\langle f, g \rangle = \int_{\partial\Omega} f(\mathbf{r}) g(\mathbf{r}) \, ds(\mathbf{r}')$. With a slight abuse of notation, we will also consider the values of the above-defined $(\mathcal{D}f)(\mathbf{r})$ and $(\mathcal{S}f)(\mathbf{r})$ at any point in $\mathbb{R}^3$, not necessarily on the boundary $\partial\Omega$. The same generalization can also be applied to $(\mathcal{D}^*f)(\mathbf{r})$, and to $(\mathcal{N}f)(\mathbf{r})$, choosing an arbitrary smooth vector field $\mathbf{n}(\mathbf{r})$.

To simplify the treatment and avoid ambiguity, we choose to work with potential functions vanishing at infinity; more precisely, we say that a function u satisfies condition $\mathcal{H}$, if simultaneously

$$\begin{cases} \lim_{r\to\infty} r\, |u(\mathbf{r})| < \infty \\ \lim_{r\to\infty} r \frac{\partial u}{\partial r}(\mathbf{r}) = 0 \end{cases}$$

where $r = \|\mathbf{r}\|$, and $(\partial u / \partial r)(\mathbf{r})$ denotes the partial derivative of u in the radial direction. The Green function G in (5) satisfies $\mathcal{H}$. The condition $\mathcal{H}$ corresponds to the physical intuition that a static field far away from all charges is zero. This goes together with the hypothesis we need in order to make our initial physical problem uniquely solvable, namely that we are only interested in the field due to sources inside our bounded volumes, i.e., inside the head.

We are now ready to state the fundamental representation theorem on which the BEM is based.

Theorem 1 (Representation Theorem): Let $\Omega \subseteq \mathbb{R}^3$ be a bounded open set with a regular boundary $\partial\Omega$. Let $u : (\mathbb{R}^3 \backslash \partial\Omega) \to \mathbb{R}$ be a harmonic function ($\Delta u = 0$ in $\mathbb{R}^3 \backslash \partial\Omega$), satisfying the $\mathcal{H}$ condition, and let further $p(\mathbf{r}) \stackrel{\text{def}}{=} \partial_{\mathbf{n}} u(\mathbf{r})$. Then

$$\begin{array}{llll} -p = & +\mathcal{N}[u] & -\mathcal{D}^*[p], & \text{for } \mathbf{r} \notin \partial\Omega \\ u = & -\mathcal{D}[u] & +\mathcal{S}[p] & \\ -p^{\pm} = & +\mathcal{N}[u] & +\left(\pm\frac{\mathcal{I}}{2} - \mathcal{D}^*\right)[p], & \text{for } \mathbf{r} \in \partial\Omega \\ u^{\pm} = & \left(\mp\frac{\mathcal{I}}{2} - \mathcal{D}\right)[u] & +\mathcal{S}[p] & \end{array}$$

$$(7)$$

where $\mathcal{I}$ denotes the identity operator.

The Theorem holds in particular for the hollow ball topology depicted in Fig. 2, i.e., for disjoint open sets $\Omega_1, \Omega_2, \Omega_3$ such that $\overline{\Omega}_1 \cup \overline{\Omega}_2 \cup \Omega_3 = \mathbb{R}^3$, separated by regular boundaries $\partial\Omega_1 \cap \partial\Omega_2 = S_1$, $\partial\Omega_2 \cap \partial\Omega_3 = S_2$, and $\partial\Omega_1 \cap \partial\Omega_3 = \emptyset$, if we set $\partial\Omega = S_1 \cup S_2$. This result will be used in Section III-G to establish the symmetric formulation.

Theorem 1 shows that any harmonic function u in $\mathbb{R}^3 \backslash \partial\Omega$ satisfying $\mathcal{H}$ is determined everywhere by its jump and the jump
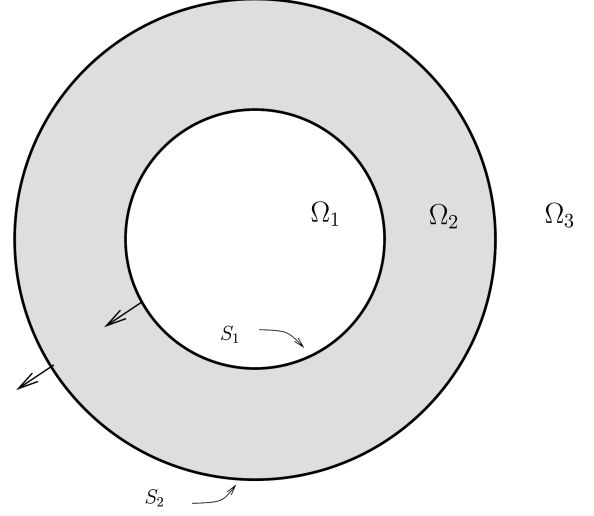

Fig. 2. Two-dimensional slice through a volume Ω_2 (delimited by surfaces S_1, S_2) with a hollow ball topology. Arrows denote the normal orientation.

of its derivative across the boundary $\partial\Omega$, whether $\partial\Omega$ is a single surface, or two surfaces as in the case of Fig. 2. This is a very deep result, showing the strong constraints imposed by the harmonicity. It helps us to understand why we can solve a three-dimensional problem by only considering quantities on a two-dimensional surface. For additional notes and a sketch of a proof, see Appendix A.

A. Single- and Double-Layer Potentials

From (7) in Theorem 1, we see that the harmonic function u can be represented using two functions $\mu = -[u]$ and $\xi = [p]$ defined on $\partial\Omega$. Historically, the $\mathcal{S}\xi$ part of (7) is called a *single-layer potential*. The single-layer potential is continuous when crossing $\partial\Omega$, while its normal derivative is not; $[\mathcal{S}\xi]_{\partial\Omega} = 0$, $[\partial_{\mathbf{n}}\mathcal{S}\xi]_{\partial\Omega} = \xi$. On the other hand, the second part, $\mathcal{D}\mu$, which is called a *double-layer potential*, jumps over $\partial\Omega$, while its normal derivative does not; $[\mathcal{D}\mu]_{\partial\Omega} = -\mu$, $[\partial_{\mathbf{n}}\mathcal{D}\mu]_{\partial\Omega} = 0$. More detail on single- and double-layer potentials is provided in Appendix A.

To apply the single-/double-layer potentials to our nested-region model in Fig. 1, we simply add up the contributions from all interfaces, $u_s = \sum_i \mathcal{S}\xi_{S_i}$, respectively, $u_d = \sum_i \mathcal{D}\mu_{S_i}$. This yields single-, respectively, double-layer potentials with the same jump properties as in the single interface case (see Appendix B). In particular, we shall need further on the following two relations, easily obtainable from (7) by additivity:

$$\partial_{\mathbf{n}} u_s^{\pm}(\mathbf{r}) = \mp \frac{\xi_{S_j}}{2} + \sum_{i=1}^{N} \mathcal{D}_{ji}^* \xi_{S_i} \quad \text{for } \mathbf{r} \in S_j \qquad (8)$$

$$u_d^{\pm}(\mathbf{r}) = \pm \frac{\mu_{S_j}}{2} + \sum_{i=1}^{N} \mathcal{D}_{ji} \mu_{S_i} \quad \text{for } \mathbf{r} \in S_j \qquad (9)$$

The operators $\mathcal{D}_{ji}^*$ and $\mathcal{D}_{ji}$ are restrictions of $\mathcal{D}^*$ and $\mathcal{D}$: they act on a function defined on S_i and yield a function defined on S_j. This convention is used consistently in the rest of this paper.

III. INTEGRAL FORMULATIONS

Let us use Theorem 1 to obtain integral formulations for the original multiple interface problem (4). We now need to cope with the presence of sources, which make the solution nonharmonic. Our starting point is a homogeneous solution v, which takes the source terms into account, but does not necessarily respect all boundary conditions. Then we add to v a harmonic function u to obtain a complete solution V which simultaneously respects the Poisson equation $\sigma_i \Delta V = f$ in all Ω_i, the boundary conditions (4), and (3). Three different ways of achieving this are described in this section. We shall always assume that V satisfies condition $\mathcal{H}$, which amounts to imposing a zero potential infinitely far from all sources.

A. Dipolar and Surface Sources

The source model most commonly used to represent electrical activity in the brain is a "current dipole"[1] [3]. It represents an infinitely small oriented source of current positioned at $\mathbf{r}_0$, with dipolar moment $\mathbf{q}$, and is defined by $\mathbf{J}_{\mathrm{dip}}(\mathbf{r}) = \mathbf{q}\,\delta_{\mathbf{r}_0}(\mathbf{r})$. The corresponding source term in the Poisson equation is $f_{\mathrm{dip}} = \nabla \cdot \mathbf{J}_{\mathrm{dip}} = \mathbf{q} \cdot \nabla \delta_{\mathbf{r}_0}$, which yields the homogeneous domain potential

$$v_{\mathrm{dip}}(\mathbf{r}) = \frac{1}{4\pi}\frac{\mathbf{q} \cdot (\mathbf{r} - \mathbf{r}_0)}{\|\mathbf{r} - \mathbf{r}_0\|^3}. \qquad (10)$$

The dipolar source is physiologically plausible in that it represents movement of charges, not their creation. At sufficiently long time scale it approximates the neuronal pulse trains.

Sources on cortex surface and perpendicular to it can be also modeled as $\mathbf{J}_{\mathrm{surf}}(\mathbf{r}) = j(\mathbf{r})\,\mathbf{n}_P(\mathbf{r})\,\delta_P(\mathbf{r})$ with scalar surface current density j on a patch P. The corresponding homogeneous potential v_{surf} is then calculated by integration over P

$$v_{\mathrm{surf}}(\mathbf{r}) = \frac{1}{4\pi}\int_{\mathbf{r}' \in P} \frac{\mathbf{n}_P(\mathbf{r}') \cdot (\mathbf{r} - \mathbf{r}')}{\|\mathbf{r} - \mathbf{r}'\|^3} j(\mathbf{r}')\,\mathrm{d}\mathbf{r}'. \qquad (11)$$

Finally, we can consider a completely general volume current density $\mathbf{J}^{\mathrm{P}}$, yielding a source term $f = \nabla \cdot \mathbf{J}^{\mathrm{P}}$ and a potential $v = -f * G$. (See, also, next Section.)

B. Homogeneous Solution

We decompose the source f from (1) into $f = \sum_{i=1}^{N} f_{\Omega_i}$ such that $f_{\Omega_i} = f \cdot 1_{\Omega_i}$, where 1_{Ω_i} is the indicator function of Ω_i (hence, $f_{\Omega_i} = 0$ outside Ω_i), $i = 1, \dots, N$. Recall that no source lies in Ω_{N+1}; we also assume that no source lies on any boundary S_i.

For each partial source term f_{Ω_i} we calculate the homogeneous medium solution $v_{\Omega_i}(\mathbf{r}) = -f_{\Omega_i} * G(\mathbf{r})$. The convolution theorem and the properties of the Green function (5) show that $\Delta v_{\Omega_i} = -f_{\Omega_i} * \Delta G = f_{\Omega_i}$. The v_{Ω_i} are harmonic in $\mathbb{R} \backslash \overline{\Omega}_i$, $i = 1, \dots, N$ and, hence, also in Ω_{N+1}. Thanks to the choice of G in (5), the functions v_{Ω_i} satisfy condition $\mathcal{H}$, provided that the f_{Ω_i} are compactly supported. This is true by construction for $\Omega_1, \dots, \Omega_N$ since each of these domains is bounded.

C. Multiple Domains

There are various ways of combining the individual homogeneous solutions v_{Ω_i} from domains Ω_i into a global homogeneous v. First we consider a function v_s constructed as

$$v_s = \sum_{i=1}^{N} \frac{v_{\Omega_i}}{\sigma_i}. \qquad (12)$$

We easily verify that it satisfies the Poisson equation $\sigma \Delta v_s = f$ in each $\Omega_i, i = 1, \dots, N$

$$\sigma \Delta v_s = \sigma \sum_{i=1}^{N} \frac{\Delta v_{\Omega_i}}{\sigma_i} = \sigma \sum_{i=1}^{N} \frac{f_{\Omega_i}}{\sigma_i} = \sum_{i=1}^{N} f_{\Omega_i} = f$$

According to the previous section, all functions v_{Ω_i}, $i = 1, \dots, N$ are harmonic in Ω_{N+1}, hence, so is v_s.

The function v_s and its derivative $\partial_{\mathbf{n}} v_s$ are continuous across each S_j. In other words, v_s satisfies the boundary conditions $[v_s]_j = 0$ and $[\partial_{\mathbf{n}} v_s]_j = 0$ for all j, but not the boundary condition $[\sigma \partial_{\mathbf{n}} v_s]_j = 0$. The function v_s will be used in the single-layer approach, Section III-D, whence the subscript s.

In a dual fashion, we would like to consider the function $\tilde{v}_d(\mathbf{r}) = \sigma^{-1}(\mathbf{r}) \sum_{i=1}^{N} v_{\Omega_i}$ that satisfies $\sigma \Delta \tilde{v}_d = f$ and the boundary condition $[\sigma \partial_{\mathbf{n}} \tilde{v}_d]_j = 0$. Unfortunately, $\tilde{v}_d$ is not properly defined in Ω_{N+1} where $\sigma = 0$. Instead, we introduce a function

$$v_d = \sum_{i=1}^{N} v_{\Omega_i} \qquad (13)$$

that satisfies the Poisson equation $\Delta v_d = f$ and the boundary conditions $[v_d]_j = 0$ and $[\partial_{\mathbf{n}} v_d]_j = 0$ on each surface S_j. The function v_d is harmonic in Ω_{N+1} for the same reasons as v_s. This function is used in the double-layer approach, Section III-E.

D. Single-Layer Approach

A natural approach for solving (1) consists in representing the potential V in a way which automatically satisfies $[V]_j = 0$ and then adjusting the harmonic part so that the remaining boundary conditions, $[\sigma \partial_{\mathbf{n}} V]_j = 0$, are satisfied as well. We consider $u_s = V - v_s$, with v_s defined in (12). By construction, u_s is harmonic in $\Omega = \Omega_1 \cup \dots \cup \Omega_N$, since in each Ω_i we have $\sigma_i \Delta u_s = \sigma_i \Delta V - \sigma_i \Delta v_s = f_{\Omega_i} - f_{\Omega_i} = 0$. It is also harmonic in Ω_{N+1}, as both V and v_s are harmonic there. Since $[V]_j = 0$ and $[v_s]_j = 0$ (Section III-C), we conclude that $[u_s]_j = 0$ across all surfaces S_j. This means that u_s is a single-layer potential for $\Omega = \Omega_1 \cup \dots \cup \Omega_{N+1}$ with the corresponding boundary $\partial \Omega = S_1 \cup \dots \cup S_N$ (cf. Section II-B).

We then use the second set of boundary conditions, $[\sigma \partial_{\mathbf{n}} V] = 0$, implying that $[\sigma \partial_{\mathbf{n}} u_s] = -[\sigma \partial_{\mathbf{n}} v_s]$. We express $[\sigma \partial_{\mathbf{n}} u_s]$ as a function of known quantities

$$[\sigma \partial_{\mathbf{n}} u_s]_j = -[\sigma \partial_{\mathbf{n}} v_s]_j = -(\sigma_j - \sigma_{j+1})\partial_{\mathbf{n}} v_s \quad \text{on } S_j \quad (14)$$

since $\partial_{\mathbf{n}} v_s$ does not "jump" across S_j (Section III-C). Equation (8) provides the normal derivative of the single-layer potential u_s. Writing $\xi_{S_j} = [\partial_{\mathbf{n}} u_s]_j$

$$[\sigma \partial_{\mathbf{n}} u_s]_j = \sigma_j \partial_{\mathbf{n}} u_s^- - \sigma_{j+1} \partial_{\mathbf{n}} u_s^+$$

$$= \frac{\sigma_j + \sigma_{j+1}}{2} \xi_{S_j} + (\sigma_j - \sigma_{j+1}) \sum_{i=1}^{N} \mathcal{D}_{ji}^* \xi_{S_i}$$

---

[1] This is a traditional name, used because the quantity $\mathbf{q}$ has the units of $[\mathrm{A} \cdot \mathrm{m}]$.

on all $S_1, \ldots, S_N$. Combining this result with (14) and dividing by $(\sigma_j - \sigma_{j+1})$ we obtain[2]

$$\partial_{\mathbf{n}} v_s = \frac{\sigma_j + \sigma_{j+1}}{2(\sigma_{j+1} - \sigma_j)} \xi_{S_j} - \sum_{i=1}^{N} \mathcal{D}_{ji}^* \xi_{S_i} \quad \text{on all } S_j. \quad (15)$$

This is a system of N integral equations in the unknown functions ξ_{S_j}. Its solution is unique up to a constant [7] (see also Appendix C). Once (15) is solved, the potential u_s is determined for $\mathbf{r} \in S_j$ as

$$u_s(\mathbf{r}) = \sum_{i=1}^{N} \mathcal{S}_{ji} \xi_{S_i}$$

and the corresponding values of V follow from $V = v_s + u_s$.

We observe that V is expressed as an exactly calculable homogeneous medium potential v_s plus a correction term u_s. If the medium is close to homogeneous, the correction is small, which helps to improve the accuracy of this method. This method is to be favored if we are interested in calculating the flow or the current. However, to obtain the potential V, an additional computation is necessary.

E. Double-Layer Approach

The double-layer approach is dual to the single-layer approach. We use a representation satisfying $[\sigma \partial_{\mathbf{n}} V]_j = 0$ by construction and then find conditions on the harmonic part to impose $[V]_j = 0$ as well. Consider a function $u_d = \sigma V - v_d$, with v_d given by (13). By construction, u_d is harmonic in $\Omega = \Omega_1 \cup \cdots \cup \Omega_N$, because in each Ω_i we have $\Delta u_d = \sigma_i \Delta V - \Delta v_d = f_{\Omega_i} - f_{\Omega_i} = 0$. It is also harmonic in Ω_{N+1}, as both V and v_d are harmonic there. Since $[\sigma \partial_{\mathbf{n}} V]_j = 0$ and $[\partial_{\mathbf{n}} v_d]_j = 0$ (Section III-C), we conclude that $[\partial_{\mathbf{n}} u_d]_j = 0$ on all surfaces S_j. This means that u_d is a double-layer potential for $\Omega = \Omega_1 \cup \cdots \cup \Omega_{N+1}$ with the corresponding boundary $\partial \Omega = S_1 \cup \cdots \cup S_N$. Equation (9) expresses the boundary values of a double-layer representation. We now use the second set of boundary conditions, $[V]_j = 0$, implying that $\sigma_{j+1}(u_d + v_d)^- = \sigma_j(u_d + v_d)^+$ for all S_j. (This is equivalent to $\sigma_j^{-1}(u_d + v_d)^- = \sigma_{j+1}^{-1}(u_d + v_d)^+$ for $\sigma \neq 0$ and a natural extension thereof for $\sigma = 0$.) We can also express $\mu_{S_i} = -[u_d] = (\sigma_{i+1} - \sigma_i)V_{S_i}$, where V_{S_i} is the restriction of V to S_i. This yields

$$v_d = \frac{\sigma_j + \sigma_{j+1}}{2} V_{S_j} - \sum_{i=1}^{N} (\sigma_{i+1} - \sigma_i) \mathcal{D}_{ji} V_{S_i} \quad \text{on each } S_j. \quad (16)$$

The function v_d defined in (13) is the solution of $\Delta v_d = f$, corresponding to a homogeneous medium with conductivity equal to one. Remembering that $\mathcal{D}_{ji} V_{S_i}(\mathbf{r}) = \int_{S_i} \partial_{\mathbf{n}'} G(\mathbf{r} - \mathbf{r}') V(\mathbf{r}') ds(\mathbf{r}')$ for $\mathbf{r} \in S_j$, we recognize in (16) the classical integral formulation used for EEG and MEG [2], [3], [17], [19], [20]. The advantage of this approach is that it solves directly for V and requires no additional postprocessing. As in the single-layer approach, the solution of the system (16) is unique up to a constant [7].

---

[2]The division by $(\sigma_j - \sigma_{j+1})$ has been done to simplify the formula. It should not be performed for small values $|\sigma_j - \sigma_{j+1}|$ in order to avoid numerical difficulties.
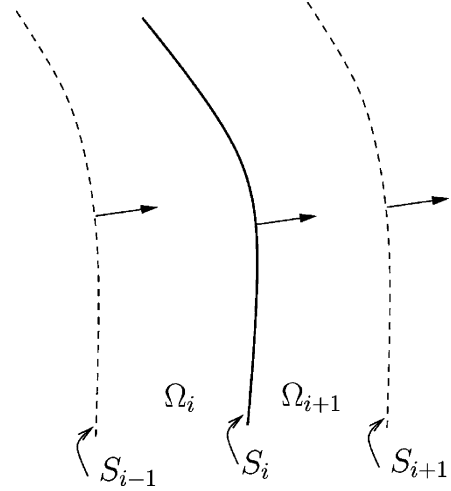

Fig. 3. A detail of the nested volume model. Normal vectors are oriented globally outward, as shown. However, when considering for example the surface S_i as the boundary of Ω_{i+1}, the orientation needs to be reversed.

F. Isolated Problem Approach

In 1989, Hämäläinen and Sarvas [13] introduced a variation on this double-layer formulation, to improve the precision of the the classical formulation, caused by the low conductivity of the skull compared to the other head tissues. This approach, called *Isolated Problem Approach* (IPA) or *Isolated Skull Approach*, is based on the same idea that improves the accuracy of the single-layer method — we express the potential V as a sum of two parts calculated separately with hopefully more precision than calculating the final result directly. In this case, we calculate first the field of the sources considering only the innermost volume and then the appropriate correction.

The IPA is not general in that it assumes the sources to be only in the innermost layer, which is not the case for the more realistic models of the head, where we want to consider sources in the cortex. Also, while it improves the precision in some cases, it reduces it in others [20]. Therefore, we shall not consider IPA in the rest of this paper.

G. Symmetric Approach

The symmetric approach uses both the single- and double-layer potentials. It is based on the classical theory of Newtonian potentials as described in [26, chapter 2], the work of Nédélec [7] and is also closely related to algorithms in [23], [24]. However, as far as we know, it has so far never been described for the EEG problem. In this approach, we consider in each $\Omega_1, \ldots, \Omega_N$ the function

$$u_{\Omega_i} = \begin{cases} V - \frac{v_{\Omega_i}}{\sigma_i}, & \text{in } \Omega_i \\ \frac{-v_{\Omega_i}}{\sigma_i}, & \text{in } \mathbb{R}^3 \backslash \overline{\Omega}_i \end{cases}.$$

Each u_{Ω_i} is harmonic in $\mathbb{R}^3 \backslash \partial \Omega_i$. Considering the nested volume model (Fig. 1), the boundary of Ω_i is $\partial \Omega_i = S_{i-1} \cup S_i$. With respect to the orientations of normals indicated in Fig. 3, the jumps of u_{Ω_i} across S_i satisfy the relations

$$[u_{\Omega_i}]_i = V_{S_i}, \quad [u_{\Omega_i}]_{i-1} = -V_{S_{i-1}}, \quad (17a)$$

and the jumps of their derivatives

$$[\partial_{\mathbf{n}} u_{\Omega_i}]_i = (\partial_{\mathbf{n}} V)_{S_i}^-, \quad [\partial_{\mathbf{n}} u_{\Omega_i}]_{i-1} = -(\partial_{\mathbf{n}} V)_{S_{i-1}}^+. \quad (17b)$$

We define $p_{S_i} = \sigma_i[\partial_{\mathbf{n}}u_{\Omega_i}]_i = \sigma_i(\partial_{\mathbf{n}}V)^-_{S_i}$. Note that since $[\sigma\partial_{\mathbf{n}}V] = 0$ from (4), we have $p_{S_i} = \sigma_i(\partial_{\mathbf{n}}V)^-_{S_i} = \sigma_{i+1}(\partial_{\mathbf{n}}V)^+_{S_i}$ at the interface S_i. As u_{Ω_i} is harmonic in $\mathbb{R}^3\backslash\partial\Omega_i$ and satisfies the condition $\mathcal{H}$, we can apply Theorem 1 to obtain the internal limit of u_{Ω_i} on S_i

$$\left(u_{\Omega_i}\right)^-_{S_i} = \frac{[u_{\Omega_i}]_{\partial\Omega_i}}{2} - \mathcal{D}_{\partial\Omega_i}[u_{\Omega_i}]_{\partial\Omega_i} + \mathcal{S}_{\partial\Omega_i}[\partial_{\mathbf{n}}u_{\Omega_i}]_{\partial\Omega_i}.$$

If we break down the jump terms across $\partial\Omega_i = S_{i-1}\cup S_i$ into two parts, corresponding to S_{i-1} and S_i, and if we take into account identities (17a), we obtain

$$\left(u_{\Omega_i}\right)^-_{S_i} = \left(V - \frac{v_{\Omega_i}}{\sigma_i}\right)^-_{S_i} = \frac{V_{S_i}}{2} + \mathcal{D}_{i,i-1}V_{S_{i-1}}$$
$$- \mathcal{D}_{ii}V_{S_i} - \sigma_i^{-1}\mathcal{S}_{i,i-1}p_{S_{i-1}} + \sigma_i^{-1}\mathcal{S}_{ii}p_{S_i}. \quad (18)$$

A similar analysis applies to $u_{\Omega_{i+1}}$. Theorem 1 gives the external limit of $u_{\Omega_{i+1}}$ on S_i

$$\left(u_{\Omega_{i+1}}\right)^+_{S_i} = -\frac{[u_{\Omega_{i+1}}]_{\partial\Omega_{i+1}}}{2} - \mathcal{D}_{\partial\Omega_{i+1}}[u_{\Omega_{i+1}}]_{\partial\Omega_{i+1}}$$
$$+ \mathcal{S}_{\partial\Omega_{i+1}}[\partial_{\mathbf{n}}u_{\Omega_{i+1}}]_{\partial\Omega_{i+1}}.$$

We substitute from (17a) for the values of $[u_{\Omega_{i+1}}]$ and $[\partial_{\mathbf{n}}u_{\Omega_{i+1}}]$ and break down the terms on $\partial\Omega_{i+1} = S_i\cup S_{i+1}$, to obtain

$$\left(u_{\Omega_{i+1}}\right)^+_{S_i} = \left(V - \frac{v_{\Omega_{i+1}}}{\sigma_{i+1}}\right)^+_{S_i}$$
$$= \frac{V_{S_i}}{2} + \mathcal{D}_{ii}V_{S_i} - \mathcal{D}_{i,i+1}V_{S_{i+1}} - \sigma_{i+1}^{-1}\mathcal{S}_{ii}p_{S_i}$$
$$+ \sigma_{i+1}^{-1}\mathcal{S}_{i,i+1}p_{S_{i+1}}. \quad (19)$$

We subtract (18) and (19); given that the functions V, $v_{\Omega_{i+1}}$ and v_{Ω_i} are continuous across S_i and their internal and external limits, hence, coincide, we get

$$\sigma_{i+1}^{-1}(v_{\Omega_{i+1}})_{S_i} - \sigma_i^{-1}(v_{\Omega_i})_{S_i}$$
$$= \mathcal{D}_{i,i-1}V_{S_{i-1}} - 2\mathcal{D}_{ii}V_{S_i} + \mathcal{D}_{i,i+1}V_{S_{i+1}} - \sigma_i^{-1}\mathcal{S}_{i,i-1}p_{S_{i-1}}$$
$$+ (\sigma_i^{-1} + \sigma_{i+1}^{-1})\mathcal{S}_{ii}p_{S_i} - \sigma_{i+1}^{-1}\mathcal{S}_{i,i+1}p_{S_{i+1}} \quad (20)$$

for $i = 1,\dots,N$. Using the same approach, we evaluate the quantities $\left(\sigma_i\partial_{\mathbf{n}}u_{\Omega_i}\right)^-_{S_i} = \left(p - \partial_{\mathbf{n}}v_{\Omega_i}\right)^-_{S_i}$ and

$\left(\sigma_{i+1}\partial_{\mathbf{n}}u_{\Omega_{i+1}}\right)^+_{S_i} = \left(p - \partial_{\mathbf{n}}v_{\Omega_{i+1}}\right)^+_{S_i}$ using Theorem 1, subtract the resulting expressions and obtain

$$(\partial_{\mathbf{n}}v_{\Omega_{i+1}})_{S_i} - (\partial_{\mathbf{n}}v_{\Omega_i})_{S_i}$$
$$= \sigma_i\mathcal{N}_{i,i-1}V_{S_{i-1}} - (\sigma_i + \sigma_{i+1})\mathcal{N}_{ii}V_{S_i} + \sigma_{i+1}\mathcal{N}_{i,i+1}V_{S_{i+1}}$$
$$- \mathcal{D}^*_{i,i-1}p_{S_{i-1}} + 2\mathcal{D}^*_{ii}p_{S_i} - \mathcal{D}^*_{i,i+1}p_{S_{i+1}} \quad (21)$$

for $i = 1,\dots,N$. Here [and in (20)] the terms corresponding to nonexisting surfaces S_0, S_{N+1} are to be set to zero. Terms involving p_{S_N} must also be set to zero, since $\sigma_{N+1} = 0$ implies $p_{S_N} = 0$.

Observe that, unlike in the previous approaches, each surface only interacts with its neighbors, at the cost of considering two sets of unknowns, V_{S_i} and p_{S_i}. Equation (20) and (21), thus, lead to a block-diagonal symmetric operator matrix (shown in (22) at the bottom of the page) representing the continuous operator version of the symmetric method. Special care is needed in writing the last block because of the conductivity $\sigma_{N+1} = 0$. We have noted $\sigma_{i,i+1}$ the sum $\sigma_i + \sigma_{i+1}$ and $\sigma_{i,i+1}^{-1}$ the sum $\sigma_i^{-1} + \sigma_{i+1}^{-1}$. Note that the vanishing conductivity $\sigma_{N+1} = 0$ is taken into account by effectively chopping off the last line and column of the matrix.

IV. DISCRETIZATION AND IMPLEMENTATION

The discretization of all the exposed integral methods can be divided into three steps: discretization of the boundaries, discretization of the unknowns, and choice of the test functions, corresponding to the choice of the error measure to discretize the equations.

A. Discretization of the Boundaries

The first step is to approximate the boundaries by surface meshes. Triangulation is used in the vast majority of cases. Higher order surface elements [22] are rarely used for the EEG problem, despite their potential to improve the modeling accuracy, because of the lack of algorithms to generate curved meshes from the available data (mostly volumes of anatomical magnetic resonance imaging (MRI) [27], [28]). As

$$\begin{bmatrix} \sigma_{1,2}\mathcal{N}_{11} & -2\mathcal{D}^*_{11} & -\sigma_2\mathcal{N}_{12} & \mathcal{D}^*_{12} & & & & & \\ -2\mathcal{D}_{11} & \sigma_{1,2}^{-1}\mathcal{S}_{11} & \mathcal{D}_{12} & -\sigma_2^{-1}\mathcal{S}_{12} & & & & & \\ -\sigma_2\mathcal{N}_{21} & \mathcal{D}^*_{21} & \sigma_{2,3}\mathcal{N}_{22} & -2\mathcal{D}^*_{22} & \cdots & & & & \\ \mathcal{D}_{21} & -\sigma_2^{-1}\mathcal{S}_{21} & -2\mathcal{D}_{22} & \sigma_{2,3}^{-1}\mathcal{S}_{22} & \cdots & & & & \\ & & \vdots & \vdots & \ddots & & & & \\ & & & & & \sigma_{N-1,N}\mathcal{N}_{N-1,N-1} & -2\mathcal{D}^*_{N-1,N-1} & -\sigma_N\mathcal{N}_{N-1,N} \\ & & & & & -2\mathcal{D}_{N-1,N-1} & \sigma_{N-1,N}^{-1}\mathcal{S}_{N-1,N-1} & \mathcal{D}_{N-1,N} \\ & & & & & -\sigma_N\mathcal{N}_{N,N-1} & \mathcal{D}^*_{N,N-1} & \sigma_N\mathcal{N}_{N,N} \end{bmatrix}$$
$$\cdot\begin{bmatrix} V_{S_1} \\ p_{S_1} \\ V_{S_2} \\ p_{S_2} \\ V_{S_3} \\ p_{S_3} \\ \vdots \\ V_{S_N} \end{bmatrix} = \begin{bmatrix} (\partial_{\mathbf{n}}v_{\Omega_1})_{S_1} - (\partial_{\mathbf{n}}v_{\Omega_2})_{S_1} \\ \sigma_2^{-1}(v_{\Omega_2})_{S_1} - \sigma_1^{-1}(v_{\Omega_1})_{S_1} \\ (\partial_{\mathbf{n}}v_{\Omega_2})_{S_2} - (\partial_{\mathbf{n}}v_{\Omega_3})_{S_2} \\ \sigma_3^{-1}(v_{\Omega_3})_{S_2} - \sigma_2^{-1}(v_{\Omega_2})_{S_2} \\ (\partial_{\mathbf{n}}v_{\Omega_3})_{S_3} - (\partial_{\mathbf{n}}v_{\Omega_4})_{S_3} \\ \sigma_4^{-1}(v_{\Omega_4})_{S_3} - \sigma_3^{-1}(v_{\Omega_3})_{S_3} \\ \vdots \\ (\partial_{\mathbf{n}}v_{\Omega_N})_{S_N} \end{bmatrix} \quad (22)$$

a triangulated surface is not regular, some caution is needed in the application of the continuous equations derived above (cf. Appendix D).

B. Discretization of the Unknowns

The second step consists in approximating the continuous unknowns V, p or ξ using a finite number of basis functions φ_i, for example $V = \sum_i v_i \varphi_i$. A classical choice is the space P0, spanned by basis functions ψ_i equal to 1 on triangle T_i and 0 elsewhere. Another possibility is the space P1, whose basis functions ϕ_i are equal to 1 on vertex i, 0 on all other vertices, and linear on each triangle. If N_v (respectively, N_t) represents the number of vertices (respectively, triangles) in the mesh, the number of P1 (respectively, P0) basis functions is N_v (respectively, N_t). For closed meshes, $N_t = 2(N_v - 2)$. Higher order basis functions are not useful with meshes composed of flat elements, the additional precision being wasted since the total error of the method becomes dominated by the geometrical error.

C. Test Functions

Third, to convert the continuous equations of discrete variables into a set of discrete equations, we integrate each of them against a set of test functions $\tilde{\varphi}_j$. The simplest choice of test functions is a Dirac mass, $\tilde{\varphi}_i = \delta_{\mathbf{x}_i}$. This method, called "collocation," is comparatively simple and fast, but often not very accurate. One normally chooses as many collocation points as unknowns. Special care is needed to evaluate the functions at nonregular points of the surface, such as vertices (see Appendix D).

Galerkin-type methods replace the pointwise equality by an equality in the mean sense. The test functions $\tilde{\varphi}_i$ are often chosen equal to the basis functions φ_i; this leads to square system matrices. There is an extra integration involved which most of the time needs to be performed numerically. Many times the integrand is singular which augments the difficulty. Galerkin methods are, hence, more difficult to implement and slower than collocation, but usually more accurate [8], [12], [20]. We shall, therefore, concentrate on Galerkin methods in the detailed treatment of the three integral formulations that follows, even though we report the results for the collocation methods as well.

D. Single-Layer Formulation

The continuous equation (15) obtained in the single-layer approach (Section III-D) is discretized using a Galerkin method, described above. The single-layer density ξ_{S_k} on S_k is represented as $\xi_{S_k}(\mathbf{r}) = \sum_i x_i^{(k)} \varphi_i^{(k)}(\mathbf{r})$, where φ_i can be either a P0 or a P1 basis function. Taking the scalar product of (15) (in which ξ_{S_k} has been discretized) with the same functions $\varphi_i^{(k)}$ yields the following set of equations:

$$\langle \partial_{\mathbf{n}} v_s, \varphi_i^{(k)} \rangle = \frac{\sigma_k + \sigma_{k+1}}{2(\sigma_{k+1} - \sigma_k)} \left(\sum_j x_j^{(k)} \langle \varphi_i^{(k)}, \varphi_j^{(k)} \rangle \right)$$
$$- \sum_{l=1}^{N} \sum_j x_j^{(l)} \langle \mathcal{D}_{lk}^* \varphi_j^{(l)}, \varphi_i^{(k)} \rangle. \quad (23)$$

The explicit matrix form is

$$\underbrace{\begin{bmatrix} J_1 + D_{11}^* & D_{12}^* & D_{13}^* & \cdots & D_{1,N}^* \\ D_{21}^* & J_2 + D_{22}^* & D_{23}^* & \cdots & D_{2,N}^* \\ D_{31}^* & D_{32}^* & J_3 + D_{33}^* & \cdots & D_{3,N}^* \\ \vdots & \vdots & \vdots & \ddots & \vdots \\ D_{N,1}^* & D_{N,2}^* & D_{N,3}^* & \cdots & J_N + D_{N,N}^* \end{bmatrix}}_{A} \begin{bmatrix} \mathbf{x}_1 \\ \mathbf{x}_2 \\ \mathbf{x}_3 \\ \vdots \\ \mathbf{x}_N \end{bmatrix}$$
$$= \begin{bmatrix} \mathbf{b}_1 \\ \mathbf{b}_2 \\ \mathbf{b}_3 \\ \vdots \\ \mathbf{b}_N \end{bmatrix} \quad (24)$$

where the matrices J (which are almost diagonal) are given by

$$(J_k)_{ij} = \frac{\sigma_k + \sigma_{k+1}}{2(\sigma_{k+1} - \sigma_k)} \langle \varphi_i^{(k)}, \varphi_j^{(k)} \rangle$$

the matrices D^* by

$$\left(D_{kl}^* \right)_{ij} = -\langle \mathcal{D}_{kl}^* \varphi_j^{(l)}, \varphi_i^{(k)} \rangle$$

and the vectors $\mathbf{b}$ and $\mathbf{x}$ by

$$(\mathbf{b}_k)_i = \langle \partial_{\mathbf{n}} v_s, \varphi_i^{(k)} \rangle, \qquad (\mathbf{x}_k)_i = x_i^{(k)}.$$

Care is needed in calculating the elements $\left(D_{kk}^* \right)_{ii}$ because of the singularity of the operator $\mathcal{D}^*$ [see (6)]. Some authors adjust the diagonal values to compensate the numerical errors of the rest of the elements using the fact that the sum of the columns of D_{kk}^* is known (see [10] for the double-layer approach). This arises from the fact that the total solid angle $\omega = 4\pi \left(\mathcal{D}_i 1 \right)(\mathbf{r})$ must be equal to 4π for all interior points, and from the physical necessity of obtaining a singular matrix (see Appendix C). The notation $\mathcal{D}_i$ indicates that the operator $\mathcal{D}$ is restricted to the ith interface. However, we prefer to set $\left(D_{kk}^* \right)_{ii}$ to 0, which is exact at regular points of flat surfaces (triangles), trivial to compute, and unlike the former approach does not obscure potential accuracy problems. We did not observe a significant difference in accuracy between the two choices.

The system matrix A is full and nonsymmetric. The elements of the matrices D^* involve double integrals over triangles of the meshes. The inner integrals can be calculated analytically for both P0 and P1 basis functions [19], [29], [30] ; the outer integrals must be calculated numerically, which is most efficiently done using a Gaussian quadrature adapted to triangles [6], [31].

Once $\mathbf{x}$ is known, the potential V is calculated directly (Section III-D) as

$$V(\mathbf{r}) = v_s(\mathbf{r}) + \sum_{l=1}^{N-1} \sum_j x_j^{(l)} \left(\mathcal{S}_{lk} \varphi_j^{(l)} \right)(\mathbf{r}) \qquad \text{for} \quad \mathbf{r} \in S_k. \quad (25)$$

Note that no approximation is involved here; if $\mathbf{x}$ is known exactly, V can be calculated exactly too.

E. Deflation

An important point to note is that the matrix A presented in (24) is singular (see Appendix C). We "deflate" it [32] using the condition $\langle \xi, 1 \rangle = 0$ (see Appendix C). For the commonly used basis functions satisfying the partition of unity property[3], this is equivalent to $\sum_i x_i^{(k)} = 0$ on each S_k, and thus $\sum_{ik} x_i^{(k)} = 0$.

[3]Their sum is equal to 1 everywhere.

To impose this, we replace A with $A' = A + \omega \mathbf{1}\mathbf{1}^T$, where ω is chosen such that A' is well conditioned. The optimal choice of ω is too costly to calculate but the value is not very critical and can be approximated [12], [33]. We use the fact that A is approximately diagonal dominant and we assume that the very first element is representative, which leads to $\omega = (A)_{11}/M$, where M is the total number of unknowns. This was found to perform acceptably well. The deflated matrix A' is regular and square and can be inverted by the usual methods.

Note that deflation is *not* equivalent to regularization that looks for a smooth solution only approximately satisfying the Maxwell equations. Instead, deflation chooses one solution from a family of equivalent ones, all satisfying the equations exactly, according to our preferences based on the physics of the problem.

F. Double-Layer Formulation

The double-layer formulation (16) is discretized using the same approach as the single-layer one, with V_{S_k} on S_k represented as $V_{S_k}(\mathbf{r}) = \sum_i x_i^{(k)} \varphi_i^{(k)}(\mathbf{r})$, where φ_i is either P0 or P1. Taking the scalar product of (16) with $\varphi_i^{(k)}$ yields

$$\langle v_d, \varphi_i^{(k)} \rangle = \frac{\sigma_k + \sigma_{k+1}}{2} \left(\sum_j x_j^{(k)} \langle \varphi_i^{(k)}, \varphi_j^{(k)} \rangle \right)$$
$$- \sum_{l=1}^{N} (\sigma_{l+1} - \sigma_l) \sum_j x_j^{(l)} \langle \mathcal{D}_{kl} \varphi_j^{(l)}, \varphi_i^{(k)} \rangle \quad (26)$$

or, in a matrix form

$$\underbrace{\begin{bmatrix} J_1 + D_{11} & D_{12} & D_{13} & \dots & D_{1,N} \\ D_{21} & J_2 + D_{22} & D_{23} & \dots & D_{2,N} \\ D_{31} & D_{32} & J_3 + D_{33} & \dots & D_{3,N} \\ \vdots & \vdots & \vdots & \ddots & \vdots \\ D_{N,1} & D_{N,2} & D_{N,3} & \dots & J_N + D_{N,N} \end{bmatrix}}_{A} \begin{bmatrix} \mathbf{x}_1 \\ \mathbf{x}_2 \\ \mathbf{x}_3 \\ \vdots \\ \mathbf{x}_N \end{bmatrix}$$
$$= \begin{bmatrix} \mathbf{b}_1 \\ \mathbf{b}_2 \\ \mathbf{b}_3 \\ \dots \\ \mathbf{b}_N \end{bmatrix} \quad (27)$$

where

$$(J_k)_{ij} = \frac{\sigma_k + \sigma_{k+1}}{2} \langle \varphi_i^{(k)}, \varphi_j^{(l)} \rangle$$
$$(D_{kl})_{ij} = -(\sigma_{l+1} - \sigma_l) \langle \mathcal{D}_{kl} \varphi_j^{(l)}, \varphi_i^{(k)} \rangle$$
$$(\mathbf{b}_k)_i = \langle v_d, \varphi_i^{(l)} \rangle, \qquad (\mathbf{x}_k)_i = x_i^{(k)}.$$

As in the single-layer case, and thanks to the duality between $\mathcal{D}$ and $\mathcal{D}^*$, the inner integrals needed to calculate elements of matrices D_{lk} have an analytical solution for both P0 and P1 basis functions [19], [29], while the outer integrals are calculated numerically [8]. The matrix is again full, nonsymmetric, and needs to be deflated, this time because the potential V is only defined up to a constant (see Appendix C). Imposing the condition $\mathcal{H}$ is impractical, and we instead impose either the mean of the potential over all surfaces to be zero, $\sum_{k=1}^{N} \sum_i x_i^{(k)} = 0$, or else the mean of the potential over the external surface to be zero, $\sum_i x_i^{(N)} = 0$. In the latter case we propose to modify (deflate)

only the bottom-right block of A, namely $J_N + D_{N,N}$. The basis functions are assumed to satisfy the partition of unity property.

The continuous V is directly accessible from the discretization equation $V(\mathbf{r}) = \sum_i x_i^{(k)} \varphi_i^{(k)}$ for $\mathbf{r} \in S_k$.

G. Symmetric Approach

The specificity of the discretization of the symmetric approach [(20) and (21)] is that both V and its derivative p are simultaneously involved as unknowns. The approximation errors for the two quantities should be asymptotically equivalent, so that the overall error is not dominated by either one. For this reason, we choose to approximate V using P1 basis functions as $V_{S_k}(\mathbf{r}) = \sum_i x_i^{(k)} \phi_i^{(k)}(\mathbf{r})$, while its derivative p is represented using the space P0, $p_{S_k}(\mathbf{r}) = \sum_i y_i^{(k)} \psi_i^{(k)}(\mathbf{r})$. Similar concerns guide our choice of test functions. We notice that the operator $\mathcal{S}$ behaves as a smoother: it increases the regularity of its argument [7] by one. The operators $\mathcal{D}, \mathcal{D}^*$ do not change it, while $\mathcal{N}$ has a derivative character: it decreases the regularity by one. The regularity is closely tied to an approximation order [34]. To balance the errors, all the scalar products should have the same approximation order. To ensure this, we multiply (20) concerning the potential (a P1 function) by P0 test functions ψ_i

$$\langle \sigma_{k+1}^{-1} v_{\Omega_{k+1}} - \sigma_k^{-1} v_{\Omega_k}, \psi_i^{(k)} \rangle$$
$$= \sum_j x_j^{(k-1)} \langle \mathcal{D}_{k,k-1} \phi_j^{(k-1)}, \psi_i^{(k)} \rangle$$
$$+ \sum_j x_j^{(k+1)} \langle \mathcal{D}_{k,k+1} \phi_j^{(k+1)}, \psi_i^{(k)} \rangle$$
$$+ (\sigma_k^{-1} + \sigma_{k+1}^{-1}) \sum_j y_j^{(k)} \langle \mathcal{S}_{kk} \psi_j^{(k)}, \psi_i^{(k)} \rangle$$
$$- \sigma_k^{-1} \sum_j y_j^{(k-1)} \langle \mathcal{S}_{k,k-1} \psi_j^{(k-1)}, \psi_i^{(k)} \rangle$$
$$- \sigma_{k+1}^{-1} \sum_j y_j^{(k+1)} \langle \mathcal{S}_{k,k+1} \psi_j^{(k+1)}, \psi_i^{(k)} \rangle$$
$$- 2 \sum_j x_j^{(k)} \langle \mathcal{D}_{kk} \phi_j^{(k)}, \psi_i^{(k)} \rangle$$

and (21) concerning the flow (a P0 function) by P1 test functions ϕ_i

$$\langle \partial_\mathbf{n} v_{\Omega_{k+1}} - \partial_\mathbf{n} v_{\Omega_k}, \phi_i^{(k)} \rangle$$
$$= \sigma_k \sum_j x_j^{(k-1)} \langle \mathcal{N}_{k,k-1} \phi_j^{(k-1)}, \phi_i^{(k)} \rangle$$
$$+ \sigma_{k+1} \sum_j x_j^{(k+1)} \langle \mathcal{N}_{k,k+1} \phi_j^{(k+1)}, \phi_i^{(k)} \rangle$$
$$- (\sigma_k + \sigma_{k+1}) \sum_j x_j^{(k)} \langle \mathcal{N}_{kk} \phi_j^{(k)}, \phi_i^{(k)} \rangle$$
$$- \sum_j y_j^{(k-1)} \langle \mathcal{D}_{k,k-1}^* \psi_j^{(k-1)}, \phi_i^{(k)} \rangle$$
$$- \sum_j y_j^{(k+1)} \langle \mathcal{D}_{k,k+1}^* \psi_j^{(k+1)}, \phi_i^{(k)} \rangle$$
$$+ 2 \sum_j y_j^{(k)} \langle \mathcal{D}_{kk}^* \psi_j^{(k)}, \phi_i^{(k)} \rangle$$

both to hold on all interfaces $k = 1, \dots, N$. This set of equations can be expressed more concisely in matrix form as shown in (28) at the bottom of the next page.

The matrix A should be truncated[4] like in (22), to account for the zero conductivity $\sigma_{N+1} = 0$.

Note that A is larger than in the single- or double-layer cases. However, it is symmetric and block-diagonal, which means that the actual number of elements to be stored is comparable or even smaller, depending on the number of interfaces. Moreover, matrices N_{kl} can be calculated at negligible costs from the intermediate results needed for calculating matrices S_{kl}, thanks to an interesting relation coming from [7, Theorem 3.3.2]

$$\langle \mathcal{N}_{kl} \varphi_i', \varphi_j' \rangle = -(\mathbf{q}_i \times \mathbf{n}_i)(\mathbf{q}_j \times \mathbf{n}_j) \langle \mathcal{S}_{kl} \psi_j^{(l)}, \psi_i^{(k)} \rangle \quad (29)$$

where $\varphi_i'(\mathbf{x}) = \left(\mathbf{q}_i \cdot \mathbf{x} + \alpha_i\right) \psi_i(\mathbf{x})$ and $\varphi_j'(\mathbf{x}) = \left(\mathbf{q}_j \cdot \mathbf{x} + \alpha_j\right) \psi_j(\mathbf{x})$ are the P1 basis functions φ restricted to one triangle.

Deflation is needed to avoid the indetermination of V. To impose a zero mean of the potential on the outermost surface, only the bottom-right block with $N_{N,N}$ is modified to $N_{N,N} + \omega \mathbf{1}\mathbf{1}^T$, using the heuristic $\omega = \left(N_{N,N}\right)_{11}/M_N$, as in Section IV-E.

H. Acceleration

As the number of mesh elements M grows, the matrix assembly time $O(M^2)$ becomes dominated by the time needed to solve the resulting linear system $O(M^3)$, e.g., by the LU decomposition. Iterative solvers [8], [9], [35] can be used instead, reducing the computation time and only accessing the matrix by matrix-vector multiplications $A\mathbf{z}$. This brings other optimization opportunities such as calculating these products approximately using a fast multipole method (FMM) [11], precorrected-fast Fourier transform [14], [36] or singular–value decomposition-based methods. Multiresolution techniques permit to reduce the number of expensive iterations on the finest level by solving first a reduced size problem and using its solution as the starting guess. Multigrid algorithms combine iterations on fine and coarse levels for even faster convergence.

Parallelizing the assembly phase is straightforward as the matrix elements can be calculated independently, even though for optimum performance the expensive calculations needed to calculate S should be reused for the calculation of N, as mentioned

[4]The bottom-right corner of A is not shown here for space reasons.

above. Parallel techniques also exist for linear system solver noniterative algorithms (SCALAPACK library).

V. EXPERIMENTS

We have implemented the single-layer, double-layer, and symmetric approaches described in this paper in both serial and parallel versions. The single- and double-layer approaches exist in three discretization variants: with the collocation method ($\tilde{\varphi}_j = \delta_{\mathbf{x}_j}$) using the P0 basis functions φ, and with the Galerkin method ($\tilde{\varphi}_j = \varphi_j$) using both P0 and P1 bases. The symmetric method is discretized using P1 basis functions for V and P0 basis functions for p. We have implemented only this choice, since with other discretizations we lose the principal advantages of the method, symmetry and accuracy. We have applied these methods first to synthetic cases where an analytical solution is known, as well as to realistically shaped head models.

Table I summarizes the different discretization choices, and indicates the labels by which they are referenced in the text and figures.

A. Speed

The speed depends strongly on the desired precision, on the optimization and acceleration techniques applied and on the specific task.[5] In our experiments, the time needed for the direct assembly of the matrix was of the order of 1–5 s for our smallest

[5]For example, one may consider that the system matrix, once assembled, can be used to solve many problems involving the same geometry. This makes the actual assembly time irrelevant.

$$\begin{bmatrix} (\sigma_1+\sigma_2)N_{11} & -2D_{11}^* & -\sigma_2 N_{12} & D_{12}^* & & & \\ -2D_{11} & (\sigma_1^{-1}+\sigma_2^{-1})S_{11} & D_{12} & -\sigma_2^{-1}S_{12} & & & \\ -\sigma_2 N_{21} & D_{21}^* & (\sigma_2+\sigma_3)N_{22} & -2D_{22}^* & -\sigma_3 N_{23} & D_{23}^* & \\ D_{21} & -\sigma_2^{-1}S_{21} & -2D_{22} & (\sigma_2^{-1}+\sigma_3^{-1})S_{22} & D_{23} & -\sigma_3^{-1}S_{23} & \\ & & -\sigma_3 N_{32} & D_{32}^* & (\sigma_3+\sigma_4)N_{33} & -2D_{33}^* & \cdots \\ & & D_{32} & -\sigma_3^{-1}S_{32} & -2D_{33} & (\sigma_3^{-1}+\sigma_4^{-1})S_{33} & \cdots \\ & & & \vdots & \vdots & & \ddots \end{bmatrix} \underbrace{\begin{bmatrix} \mathbf{x}_1 \\ \mathbf{y}_1 \\ \mathbf{x}_2 \\ \mathbf{y}_2 \\ \mathbf{x}_3 \\ \mathbf{y}_3 \\ \vdots \end{bmatrix}}_{\mathbf{w}} = \underbrace{\begin{bmatrix} \mathbf{b}_1 \\ \mathbf{c}_1 \\ \mathbf{b}_2 \\ \mathbf{c}_2 \\ \mathbf{b}_3 \\ \mathbf{c}_3 \\ \vdots \end{bmatrix}}_{\mathbf{z}}$$

$$\underbrace{}_{A}$$

with

$$(N_{kl})_{ij} = \langle \mathcal{N}_{kl} \phi_j^{(l)}, \phi_i^{(k)} \rangle \qquad (S_{kl})_{ij} = \langle \mathcal{S}_{kl} \psi_j^{(l)}, \psi_i^{(k)} \rangle$$

$$(D_{kl})_{ij} = (D_{lk}^*)_{ji} = \langle \mathcal{D}_{kl} \phi_j^{(l)}, \psi_i^{(k)} \rangle$$

$$(\mathbf{b}_k)_i = \langle \partial_\mathbf{n} v_{\Omega_k} - \partial_\mathbf{n} v_{\Omega_{k+1}}, \phi_i^{(k)} \rangle \qquad (\mathbf{c}_k)_i = \langle \sigma_{k+1}^{-1} v_{\Omega_{k+1}} - \sigma_k^{-1} v_{\Omega_k}, \psi_i^{(k)} \rangle$$

$$(\mathbf{x}_k)_i = x_i^{(k)} \qquad (\mathbf{y}_k)_i = y_i^{(k)}. \tag{28}$$

head mesh of 3×42 vertices, to several minutes to assemble the matrices of 4486×4486 elements, corresponding to the meshes of 3×642 vertices, up to about 2 h for the matrices of $17\,926 \times 17\,926$, corresponding to meshes of 3×2562 vertices. Using a parallel code on a cluster of workstations speeds the assembling proportionally to the number of processors with a high efficiency. The time needed to solve the linear system of equations varied between 10 ms and 2 h for the same cases. Generally, the assembly time grows quadratically with the number of degrees of freedom, and the solution time as a third power. Collocation methods can be 10 or more times faster than the Galerkin method, depending on the numerical integration method used and the number of integration points needed to get the required accuracy. The single-layer method is more costly than the corresponding double-layer method,[6] as two matrices need to be assembled, the matrix A in (24) in order to solve for the single-layer density, and an additional matrix in order to integrate the potential from (25).

B. Spherical Head Models

The first part of our tests was performed on triangulated spherical surfaces. The choice of a spherical geometry has the advantage that an analytical solution is available [20], [37], [38], thus making it possible to evaluate the accuracy of the different methods. The spherical surfaces were triangulated with progressively finer meshes of 42, 162, and 642 vertices per layer.[7] We used three concentric spheres with radii 0.87, 0.92, and 1.0, delimiting volumes with conductivities 1.0, 0.0125, 1.0, and 0.0, from inside toward outside. The sources were unitary current dipoles oriented as $[1\ 0\ 1]/\sqrt{2}$ and placed at distances $r = 0.425$, 0.68, 0.765, 0.8075, and 0.8415 from the center on the x axis.

We chose to evaluate the analytical solution at triangle centers for the P0 methods and at vertex points for the others. This disadvantages Galerkin methods but it is close to actual use. We then calculated the relative ℓ_2 error $\|\mathbf{v}_{\text{anal}} - \mathbf{v}_{\text{num}}\|_{\ell_2} / \|\mathbf{v}_{\text{anal}}\|_{\ell_2}$, making sure that both $\mathbf{v}_{\text{anal}}$ and $\mathbf{v}_{\text{num}}$ had zero means prior to comparison. Note that some authors linearly scale $\mathbf{v}_{\text{num}}$ to obtain the best fit [10]. This obviously significantly reduces the reported error but is difficult to justify in the context of evaluating the accuracy of a method.

We have also made some experiments using a single sphere model, not shown here because of lack of space and because it does not correspond to a plausible head model. Note that in this case the symmetric model is disadvantaged by using only the operator $\mathcal{N}$.

1) Error Versus Dipole Position: The first set of experiments (Fig. 4) shows how the accuracy decreases when the current dipole source approaches the surface of discontinuity. We observe that the symmetric approach is much less affected than the other methods.

2) Error Versus Mesh Density: For a fixed source position ($r = 0.765$), the error decreases as the mesh is refined (Fig. 5). We observe that while both collocation variants produce the
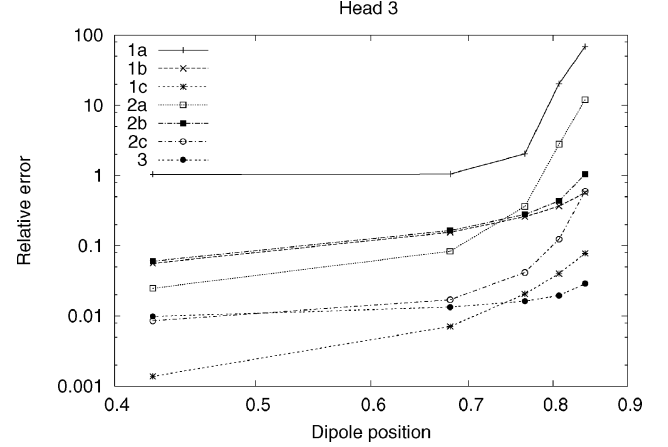
---

[6]The precise ratio depends on the discretization used.

[7]Finer meshes were avoided in this set of experiments because of memory and time limitations so that a serial direct solver could be used for most reproducible results.

Fig. 4. The relative error versus the dipole position r for meshes with 642 vertices per sphere. The label 1 (respectively, 2) refers to single-layer (respectively, double-layer) potential, and the label 3 refers to the symmetric formulation, as explained in Table I.
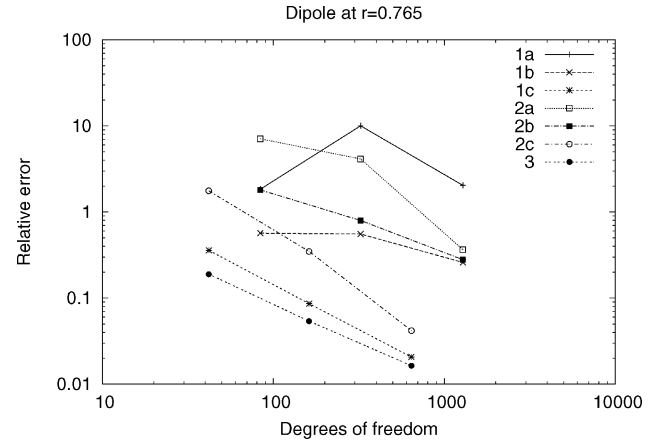

Fig. 5. The relative error versus the number of the degrees of freedom of the solution for the dipole source at $r = 0.765$. Refer to Table I for the meaning of the labels. Both P0 collocation methods in the three-sphere case are outside their area of applicability and do not provide meaningful results.

largest errors (results are completely unreliable), Galerkin methods based on P0 approximations are better, and the best results are provided by the P1 methods, namely by the symmetric formulation. Moreover, the slope of the decrease of the error with mesh size is steeper for P1-based methods, a benefit of their higher approximation order.

3) Error Versus Conductivity: The accuracy of all implemented methods depends on the ratio of conductivities between the second layer (representing the skull) and the neighboring volumes (representing brain and scalp). To display this behavior, we have created additional head models with conductivities of the three volumes 1.0, σ, 1.0, with σ ranging between 1/2 and 1/1000. Fig. 6 shows that when the conductivity ratio σ becomes small, the precision of the single- and double-layer methods drops. The symmetric method displays a clear advantage over the others since, on the contrary, its accuracy increases as $\sigma \to 0$. This is a valuable result in the context of human head modeling where $\sigma \approx 0.01$.
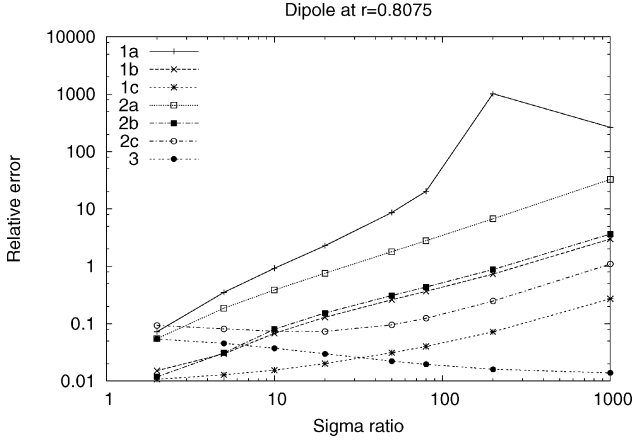
Fig. 6. The relative error versus the ratio of conductivities between neighboring layers, for dipole at $r = 0.8075$ and mesh of 642 vertices. Refer to Table I for the meaning of the labels.

C. Realistic Meshes

We generated a realistic four-layer model of the head with about 13 000 points and 26 000 faces.[8] Fig. 7 shows the potential field created by a dipole close to a cortex surface using a parallel implementation of our algorithm. This gives an indication of the complexity of the model we are currently able to process. The cortex surface contains 4960 points and the average size of the triangles' edges is 5 mm. The simulations have been performed with a dipole located inside at roughly 10 mm from this surface. The total computation took close to 6 h on a cluster of 30 PCs. It required of the order of 1000 iterations.

We used decimated versions of the same head model to compare the time and memory requirements of the different methods in this realistic setting. We had to make several simplifications in order to make this comparison possible. We only included P1 discretizations of the single- and double-layer methods because they are the most comparable with the symmetric variant in terms of representation. The superior accuracy of the Galerkin method for a majority of applications is widely recognized [8], [12], [20]. In order to obtain reliable timing results, we chose to use the sequential[9] direct[10] solver, which consequently limits the maximum mesh sizes we could process. Even so, the timing results fluctuate widely[11] and should only be regarded as indicative. Regarding accuracy comparisons, as we had no way of knowing the *ground truth* solution, we arbitrarily picked one of the three methods (the double-layer) and used its results at the finest mesh as a reference. Results at other resolutions were interpolated on the finest mesh, and the relative ℓ_2 norm $\|\mathbf{x} - \mathbf{x}_{\text{ref}}\|/\|\mathbf{x}_{\text{ref}}\|$ was used to measure accuracy (see Table II).

In order for the comparison to be meaningful, given that the reference solution was picked as one of the three solutions for

---

[8]The authors thank G. Adde and F. Segonne for preparing the hierarchical meshes from the MRI data.

[9]The timings on the cluster of PCs vary widely because we have no control over the assignment of our task to different processors and over the load imposed by other users.

[10]The number of iterations of the iterative method varies strongly with the stopping threshold, conditioning of the matrix, and other similar effects.

[11]Most likely because of the virtual memory effect. We have used the total elapsed time ("wall time") as opposed to the "CPU time" as the latter seemed to be less relevant.

the finest discretization, we had to ensure that the other two solutions were very close to that reference, otherwise there would be no reason to believe that the so-called reference should have any relationship with the true solution. The mesh size had to be increased until this requirement was met, and this proved to be difficult because of the mesh size restriction imposed by the sequential direct solver. We had to reduce the number of layers in the model, from four down to two, to increase the separation between layers, and to use a deep dipole. At convergence, the results obtained by the three methods differed in relative ℓ_2 norm by roughly 0.05 (5%) for the two-layer model.

We also ran computations on a three-layer model, but in that case, the relative errors between results at the finest discretization were as high as 20%. It would have required even finer meshes to achieve the same relative accuracy as in the two-layer case and it was not possible for the reasons indicated above. This is the reason why the accuracy results in Table II *(bottom)* compare each method to its own result at the finest discretization.

D. Discussion

A meaningful comparison of the various techniques is difficult. First, one must bear in mind that they use different number of degrees of freedom to perform the calculations, which moreover is not necessarily identical to the number of degrees of freedom used to express the solution. More specifically, for a (closed) mesh with N_v vertices, P1 methods involve N_v unknowns, P0 based methods use about $2N_v$ of them, while the symmetric method with P0/P1 discretization uses about $3N_v$ unknowns, but only N_v degrees of freedom to express the solution V.

In the case of the spherical models with three layers where the ground truth is known analytically, Fig. 4 shows that for a dipole far from an interface, the single-layer method performs best. This probably comes from the fact that it represents the solution as an exact term plus a correction. When the dipole moves closer to the interface, the symmetric method yields the best results. Fig. 5 shows that the symmetric method is less sensitive than the single-layer and the double-layer method to a decrease in the quality of the description of the geometry. Finally, Fig. 6 indicates that when the ratio of conductivities between neighboring layers is between roughly 2 and 10 the single-layer method performs best, followed by the symmetric and the traditional double-layer methods, while when this ratio grows larger than 15, the new symmetric method is clearly ahead of the single- and double-layer methods.

As stated above, in the case of the much more realistic model of Fig. 7 the comparison between the methods is more difficult since the ground-truth data is unavailable. Nevertheless, all three methods were implemented within the same programming framework, using the same basic functional blocks, and we can learn a number of things from the results shown in Table II *(top)*. It is interesting to note that the symmetric method is *less* computationally demanding than the alternatives. As already mentioned, this comes from the fact that many of the computations to assemble the system matrix of the symmetric method can be reused, which does not happen for the other methods. Also, integrating the D elements in the symmetric method with P0 and P1 basis functions is easier (the integrand is easier to evaluate) than integrating with respect to two P1 functions, as it happens
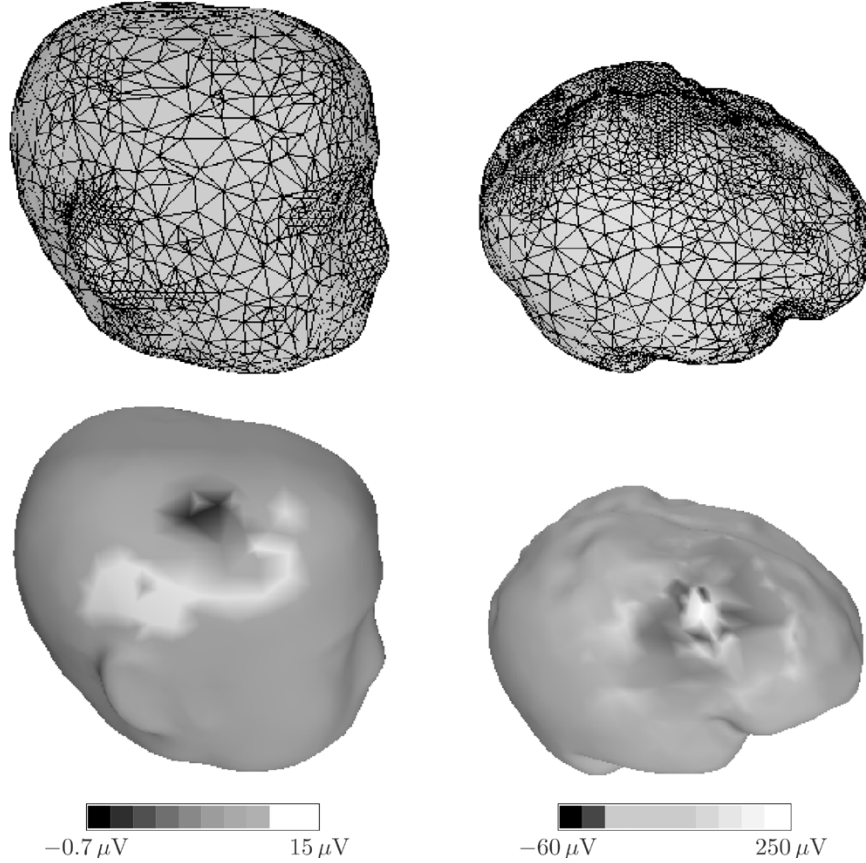
Fig. 7. *Top:* We have used a realistic four-layer model of the head with about 13 000 points and 26 000 faces. We show the surfaces corresponding to the skin *(left)* and to the cortex *(right)*. *Bottom:* We have calculated the potential field of a dipole close to a cortex surface using a parallel implementation of our algorithm. We show the electric potential on the skin *(left)* and on the cortex *(right)*.

in the D elements for the single- and double-layer P1 implementations. The matrix factorization is slower for the symmetric method due to its larger matrix size. However, for the number of unknowns considered this is compensated by the fast assembly.

As far as accuracy is concerned, we see from the last three columns of Table II *(top)* that when the number of vertices decreases from 2000 to 200, the performances of all three methods degrade similarly. The symmetric method outperforms the others for coarse meshes, despite of being disadvantaged because the double-layer method was chosen as a reference. The accuracy results for three-layer realistic meshes (Table II *(bottom)*) indicate a good convergence trend of each method, even though, as we have seen, still higher resolution meshes would be needed to make all of them converge to a common solution. This only highlights the difficulties with solving the EEG forward problem on rough (realistic) surfaces and supports our claim that much finer meshes will have to be used.

VI. CONCLUSION

We have presented a conceptual framework for BEMs in EEG which is based on a theorem (Theorem 1) that characterizes harmonic functions defined on the complement of a bounded smooth surface. This theorem has allowed us to cast the previous approaches in a unified setting and to develop two new approaches corresponding to different ways of looking at the same theorem. Specifically, we have shown that the

classical integral formulation that has been used during the last 30 years for EEG and MEG calculations by the BEM and is based on a double-layer potential is not the only one possible. We have developed a dual approach which involves a single-layer potential and proposed a symmetric formulation, which combines single- and double-layer potentials, and is new to the field of EEG, although it has been applied to other problems in electromagnetism [23], [24]. The three methods have been evaluated numerically using a spherical geometry with known analytical solution, and the symmetric formulation achieves a significantly higher accuracy than the alternative methods. Interestingly enough, the next best method does not seem to be the "traditional" double-layer method but rather the dual single-layer approach. Additionally, we have presented results with realistically shaped meshes. Beside providing a better understanding of the theoretical foundations of BEM, our approach appears to lead also to more efficient algorithms.

It is appealing by its symmetry and its superior accuracy in semi-realistic geometry. The precise theoretical analysis of the accuracy performance of the different methods is difficult because of the number of factors involved and remains to be done, although some partial results can be found in [7], [25], and [39].

The main benefit of using the proposed approach is that the error increases much less dramatically when the current sources approach a surface where the conductivity is discontinuous. This implies that we are able to reduce the number of mesh elements in a usable model of the human cortex with a realistic

TABLE II

COMPARISON OF THE SINGLE-LAYER *(1C)*, DOUBLE-LAYER *(2C)*, AND SYMMETRIC *(3)* METHODS APPLIED ON A SET OF PROGRESSIVELY FINER REALISTICALLY SHAPED HEAD MODELS WITH VARYING NUMBER OF VERTICES AND FACES. THE TABLES SHOW THE TOTAL NUMBER OF UNKNOWNS, THE ASSEMBLY TIME FOR SYSTEM MATRICES, THE TIME NEEDED FOR THEIR (LU) FACTORIZATION AND THE ESTIMATION OF THE ACHIEVED RELATIVE ACCURACY (SEE TEXT). IN THE TWO-LAYER MODEL (TOP) WE USED THE DOUBLE-LAYER METHOD AS A REFERENCE AS ALL THE METHODS CONVERGE CLOSE TO A COMMON SOLUTION. IN THE THREE-LAYER MODEL (BOTTOM) WE COMPARED EACH METHOD WITH ITS OWN RESULT ON THE FINEST MESH BECAUSE THEIR RESULTS, EVEN AT THE HIGHER RESOLUTION OF 1000 POINTS PER LAYER, WERE STILL TOO DIFFERENT. N/A (NOT APPLICABLE) INDICATES THAT THIS SOLUTION IS CHOSEN AS THE GROUND-TRUTH

Two-layer head model

vertices	faces	Degrees of freedom			Assembly time [s]			Factorization time [s]			Estimated accuracy (rel.)		
		1c	2c	3	1c	2c	3	1c	2c	3	1c	2c	3
200	196	200	200	396	47	47	10	0	0	0	0.152	0.153	0.132
400	792	400	400	796	201	194	50	0	0	4	0.109	0.106	0.092
600	1192	600	600	1196	461	656	155	1	1	10	0.090	0.088	0.078
800	1592	800	800	1596	833	951	426	1	2	24	0.080	0.081	0.072
1000	1992	1000	1000	1996	2014	1968	543	2	2	52	0.070	0.070	0.064
1200	2392	1200	1200	2396	2904	2839	1374	2	3	70	0.067	0.060	0.062
1400	2792	1400	1400	2796	3959	3582	1807	3	4	92	0.062	0.065	0.059
1600	3192	1600	1600	3196	4045	4081	3688	4	5	108	0.057	0.041	0.053
1800	3592	1800	1800	3596	8101	7915	4222	5	5	150	0.055	0.029	0.051
2000	3992	2000	3000	3996	9395	10462	4828	12	12	333	0.051	N/A	0.049

Three-layer head model

vertices	faces	Degrees of freedom			Assembly time [s]			Factorization time [s]			Estimated accuracy (rel.)		
		1c	2c	3	1c	2c	3	1c	2c	3	1c	2c	3
300	588	300	300	692	106	107	24	1	1	3	5.094	2.527	0.911
600	1188	600	600	1392	437	438	122	5	5	11	2.433	2.243	0.796
900	1788	900	900	2092	1015	1027	335	7	7	28	1.392	1.278	0.669
1200	2388	1200	1200	2792	1800	1835	578	10	9	53	1.178	0.712	0.600
1500	2988	1500	1500	3492	2853	2881	1153	15	16	91	1.907	1.579	0.513
1800	3588	1800	1800	4192	6385	4282	1727	17	17	136	0.555	0.285	0.368
2100	4188	2100	2100	4892	6191	7524	2615	26	29	188	0.282	0.258	0.260
2400	4788	2400	2400	5592	9647	11644	3694	35	33	262	0.153	0.227	0.188
2700	5388	2700	2700	6292	14416	14752	6842	48	49	1033	0.064	0.116	0.096
3000	5988	3000	3000	6992	13389	14618	8477	57	56	1346	N/A	N/A	N/A

geometry [40]. This has the effect of bringing the idea of accurate electromagnetic simulation of the human brain much closer to what can be achieved with today's technology. Nevertheless, advanced acceleration techniques will still have to be used both at the algorithm and implementation levels before this idea can be really instantiated [11], [41].

Future work includes a better understanding of the accuracy improvements and extensions of the method.

APPENDIX

We recall some basic identities between surface and volume integrals involving vector fields, leading to the Representation Theorem 1. Note that in this appendix we use an explicit integral notation for didactic purposes, while in the body of the paper we have privileged the conciseness of the operator notation (6).

A. Representation Theorems

Consider a simplified version of Problem (1): the Poisson problem $\Delta u = f$. It is well-known that the so-called Green function (5) is its fundamental solution, i.e., $-\Delta G = \delta_0$ in $\mathbb{R}^3$ in the distributional sense, where δ_0 is the Dirac mass at the origin. By translation invariance, we have

$$-\Delta_{\mathbf{r}} G(\mathbf{r} - \mathbf{r}') = \delta_0(\mathbf{r} - \mathbf{r}') = \delta_{\mathbf{r}'} \qquad (30)$$

where the notation $\Delta_{\mathbf{r}}$ signifies that partial derivatives are taken with respect to the variable $\mathbf{r}$, and $\delta_{\mathbf{r}'}$ is a Dirac mass centered at $\mathbf{r}'$.

There are many fundamental solutions to the Poisson problem, but the Green function (5) is the only one with radial symmetry (a function of the radius $r = \|\mathbf{r}\|$) and vanishing at infinity ($r \to \infty$).

Given a bounded and compact open set $\Omega \subseteq \mathbb{R}^3$ with a regular boundary $\partial\Omega$ which may not be connected, the divergence theorem $\int_\Omega \nabla \cdot \mathbf{g}(\mathbf{r}') \, d\mathbf{r}' = \int_{\partial\Omega} \mathbf{g}(\mathbf{r}') \cdot d\mathbf{s}(\mathbf{r}')$, where $d\mathbf{s}(\mathbf{r}') = \mathbf{n}'(\mathbf{r}') ds(\mathbf{r}')$, relates the integral over a volume Ω with a surface integral over its boundary $\partial\Omega$. For scalar distributions u, v, substituting $\mathbf{g} = u \nabla v$ yields the first Green identity $\int_{\partial\Omega} u \nabla v \cdot d\mathbf{s}(\mathbf{r}') = \int_\Omega \nabla u \cdot \nabla v + u \Delta v \, d\mathbf{r}'$. Exchanging u, v and subtracting the resulting equations gives the second[12] Green identity [42]

$$\int_\Omega u\Delta v - v\Delta u \, d\mathbf{r}' = \int_{\partial\Omega} \big(u\nabla v - v\nabla u\big) \cdot d\mathbf{s}(\mathbf{r}')$$
$$= \int_{\partial\Omega} u\partial_{\mathbf{n}'}v - v\partial_{\mathbf{n}'}u \, ds(\mathbf{r}')$$

where $\mathbf{n}$ is normal to $\partial\Omega$, pointing outward (from Ω to its complement $\Omega^c \equiv \mathbb{R}^3 \backslash \overline{\Omega}$), and is denoted $\mathbf{n}'$ when considered at position $\mathbf{r}'$. We now choose u to be a harmonic function ($\Delta u = 0$) in Ω, and $v(\mathbf{r}) = -G(\mathbf{r} - \mathbf{r}')$. Using (30) we obtain the third Green identity [6] below, in which $(\partial_{\mathbf{n}}u)^-$ and u^- denote boundary values taken on the inner side of the boundary with respect to the normal field $\mathbf{n}$

$$\int_{\partial\Omega} G(\mathbf{r} - \mathbf{r}') \, (\partial_{\mathbf{n}'}u)^-(\mathbf{r}') - \partial_{\mathbf{n}'}G(\mathbf{r} - \mathbf{r}') \, u^-(\mathbf{r}') \, ds(\mathbf{r}')$$
$$= \begin{cases} u(\mathbf{r}), & \text{if } \mathbf{r} \in \Omega \\ \frac{u^-(\mathbf{r})}{2}, & \text{if } \mathbf{r} \in \partial\Omega \\ 0, & \text{otherwise} \end{cases} \quad (31)$$

[12]Sometimes called the third. The numbering of Green identities varies among authors.

This important result shows that a harmonic function u inside a volume Ω is completely determined by its internal boundary values and those of its normal derivative. To make the notation more compact, we define

$$\mathcal{P}_{S,\mathbf{n}}^{\pm}(u) = \int_S G(\mathbf{r}-\mathbf{r}')(\partial_{\mathbf{n}'}u)^{\pm}(\mathbf{r}') - \partial_{\mathbf{n}'}G(\mathbf{r}-\mathbf{r}')u^{\pm}(\mathbf{r}')\mathrm{d}s(\mathbf{r}')$$

and

$$\chi_{\Omega}\,u(\mathbf{r}) = \begin{cases} u(\mathbf{r}), & \text{if } \mathbf{r} \in \Omega \\ \lim\limits_{\mathbf{r}'\to\mathbf{r},\mathbf{r}'\in\Omega} \dfrac{u(\mathbf{r}')}{2}, & \text{if } \mathbf{r} \in \partial\Omega \\ 0, & \text{if } \mathbf{r} \in \Omega^c \end{cases}.$$

Then (31) can be written as

$$\mathcal{P}_{\partial\Omega,\mathbf{n}}^{-}(u) = \chi_{\Omega}\,u. \tag{32}$$

Note that if $\mathbf{r} \in \partial\Omega$, $\lim\limits_{\mathbf{r}'\to\mathbf{r},\mathbf{r}'\in\Omega} u(\mathbf{r}') = u^-(\mathbf{r})$ with respect to a normal field $\mathbf{n}$ on $\partial\Omega$ pointing outside Ω. This is the orientation assumed on the left-hand sides of (31) and (32). Considering a normal vector field $\mathbf{n}_- = -\mathbf{n}$ which now points *inside* the domain Ω, then partial derivatives change signs, and the third Green identity (31) becomes

$$-\int_{\partial\Omega} G(\mathbf{r}-\mathbf{r}')(\partial_{\mathbf{n}_-}u)^+(\mathbf{r}') - \partial_{\mathbf{n}_-}G(\mathbf{r}-\mathbf{r}')u^+(\mathbf{r}')\mathrm{d}s(\mathbf{r}')$$

$$= \begin{cases} u(\mathbf{r}), & \text{if } \mathbf{r} \in \Omega \\ \dfrac{u^+(\mathbf{r})}{2}, & \text{if } \mathbf{r} \in \partial\Omega \\ 0, & \text{otherwise} \end{cases}$$

the $'+'$ superscript indicating that the values of u and its normal derivative must this time be considered on the side *toward* which the normal $\mathbf{n}_-$ is pointing. Therefore, for an inward-pointing normal field

$$-\mathcal{P}_{\partial\Omega,\mathbf{n}_-}^{+}(u) = \chi_{\Omega}\,u.$$

Note that χ_{Ω} is intrinsic to Ω, in the sense that it is independent of any normal orientation on $\partial\Omega$.

Interestingly, the third Green identity (31) is also valid for a hollow ball topology such as depicted in Fig. 2 as $\Omega = \Omega_2$ with a boundary consisting of two non connected parts, S_1 and S_2.

The relation (32) supposes that the normal field $\mathbf{n}$ points outside the domain Ω. This is not the case in Fig. 2, where the normal field on S_1 (which we call $\mathbf{n}_1$) points inwards, whereas the normal field on S_2 (which we call $\mathbf{n}_2$) points outwards. Decomposing $\partial\Omega = S_1 \cup S_2$, and using the above considerations on the sign of the normal, one can write

$$\chi_{\Omega}u = -\mathcal{P}_{S_1,\mathbf{n}_1}^{+}(u) + \mathcal{P}_{S_2,\mathbf{n}_2}^{-}(u). \tag{33}$$

Let us now consider a bounded volume Ω with the topology of a sphere. We take its connected unbounded complement $\Omega^c = \mathbb{R}^3\backslash\overline{\Omega}$ and derive the third Green formula for a function u harmonic in Ω^c and satisfying $\mathcal{H}$. To do this, we consider the (bounded) intersection of Ω^c with a ball B_R of radius R surrounding Ω, as shown in Fig. 8. The volume $\Omega^c \cap B_R$ has a hollow ball topology and the Green identities hold. As R tends to infinity, the contribution on ∂B_R becomes negligible thanks to the fact that both G and u satisfy condition $\mathcal{H}$. This shows that the third Green identity (31) is also valid in an unbounded
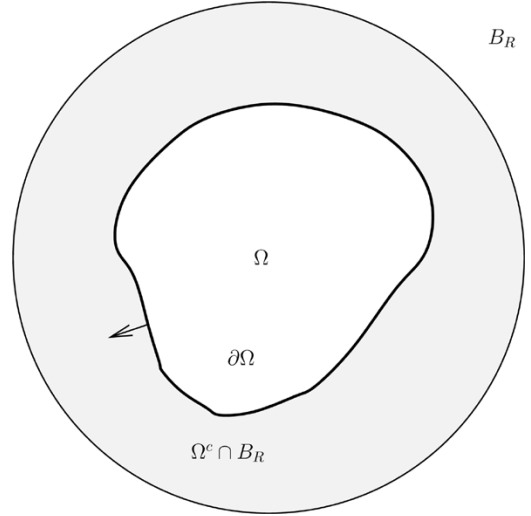

Fig. 8. Two-dimensional slice through a volume Ω enclosed within a growing ball B_R, yielding a bounded volume $\Omega^c \cap B_R$ with a hollow ball topology.

space Ω^c, for harmonic functions u satisfying $\mathcal{H}$. It can be written in the compact form

$$\chi_{\Omega^c}\,u = -\mathcal{P}_{\partial\Omega,\mathbf{n}}^{+}(u). \tag{34}$$

Combining the third Green identities for Ω and Ω^c yields the following well-known classical representation theorem, see [6], [7] for a complete proof.

Theorem 2 (Representation Theorem for u): Let $\Omega \subseteq \mathbb{R}^3$ be a bounded open set with a regular boundary $\partial\Omega$ and a connected complement space. Let $u : (\Omega \cup \Omega^c) \to \mathbb{R}$ be a function harmonic ($\Delta u = 0$) in both Ω and Ω^c, satisfying the $\mathcal{H}$ condition, and let further $p(\mathbf{r}') \overset{\text{def}}{=} p_{\mathbf{n}'}(\mathbf{r}') = \partial_{\mathbf{n}'}u(\mathbf{r}')$, where $\mathbf{n}'$ is the outward unit normal of $\partial\Omega$ at point $\mathbf{r}'$. Then for $\mathbf{r} \notin \partial\Omega$ the following representation holds:

$$u(\mathbf{r})$$
$$= \int_{\partial\Omega} -\partial_{\mathbf{n}'}G(\mathbf{r}-\mathbf{r}')[u]_{\partial\Omega}(\mathbf{r}') + G(\mathbf{r}-\mathbf{r}')[p]_{\partial\Omega}(\mathbf{r}')\mathrm{d}s(\mathbf{r}') \tag{35a}$$

and for $\mathbf{r} \in \partial\Omega$

$$u^{\pm}(\mathbf{r}) = \mp\frac{[u]_{\partial\Omega}}{2}$$
$$+ \int_{\partial\Omega} -\partial_{\mathbf{n}'}G(\mathbf{r}-\mathbf{r}')[u]_{\partial\Omega}(\mathbf{r}') + G(\mathbf{r}-\mathbf{r}')[p]_{\partial\Omega}(\mathbf{r}')\mathrm{d}s(\mathbf{r}'). \tag{35b}$$

The theorem shows that a function u harmonic in $\Omega \cup \Omega^c$ and satisfying $\mathcal{H}$ is completely determined by the jumps of $[u]$ and $[\partial_{\mathbf{n}}u]$ on the interface $\partial\Omega$. Observe that u from (35a) converges to $(u^+ + u^-)/2$ on $\partial\Omega$, while the value of u jumps when crossing the boundary. This is shown by the term $\mp[u]_{\partial\Omega}/2$ in (35b).

The *single-layer potential* [the second part of (35a)] is given explicitly as

$$u_s(\mathbf{r}) = \int_{\partial\Omega} G(\mathbf{r}-\mathbf{r}')\xi(\mathbf{r}')\,\mathrm{d}s(\mathbf{r}') \tag{36}$$

while the *double-layer potential* [the first part of (35a)] is written as

$$u_d(\mathbf{r}) = \int_{\partial\Omega} \partial_{\mathbf{n}'}G(\mathbf{r}-\mathbf{r}')\mu(\mathbf{r}')\,\mathrm{d}s(\mathbf{r}'). \tag{37}$$

The function ξ corresponds to a charge density distribution on $\partial\Omega$, while μ may be viewed as a dipole density. Both potentials (36), (37) satisfy the Laplace equation $\Delta u = 0$ in $\Omega \cup \Omega^c$ and also satisfy the condition $\mathcal{H}$. Remarkably, with arbitrary functions ξ, μ from $C^0(\partial\Omega)$, both (36) and (37) yield a harmonic function in $C^2(\Omega \cup \Omega^c)$.

The single-layer potential is continuous with respect to $\mathbf{r}$, in particular when crossing the boundary $\partial\Omega$. On the other hand, its normal derivative is discontinuous when crossing $\partial\Omega$. As proved in [7], the limit values on both sides are

$$p_{\mathbf{n}}^{\pm}(\mathbf{r}) = \partial_{\mathbf{n}} u^{\pm}(\mathbf{r})$$
$$= \mp \frac{\xi(\mathbf{r})}{2} + \int_{\partial\Omega} \partial_{\mathbf{n}} G(\mathbf{r} - \mathbf{r}') \xi(\mathbf{r}') \, \mathrm{d}s(\mathbf{r}') \text{ for } \mathbf{r} \in \partial\Omega.$$

The double-layer potential enjoys the opposite properties. It has a discontinuity when crossing $\partial\Omega$ and the corresponding limit values on both sides of $\partial\Omega$ are

$$u^{\pm}(\mathbf{r}) = \pm \frac{\mu(\mathbf{r})}{2} + \int_{\partial\Omega} \partial_{\mathbf{n}'} G(\mathbf{r} - \mathbf{r}') \mu(\mathbf{r}') \, \mathrm{d}s(\mathbf{r}') \text{ for } \mathbf{r} \in \partial\Omega. \tag{38}$$

The normal derivative of a double-layer potential is continuous when crossing $\partial\Omega$. Taking the derivative of (37) in the direction $\mathbf{n}$ at $\mathbf{r}$, we write

$$p(\mathbf{r}) = p_{\mathbf{n}}(\mathbf{r}) = \partial_{\mathbf{n}} u(\mathbf{r}) = \int_{\partial\Omega} \partial_{\mathbf{n},\mathbf{n}'}^2 G(\mathbf{r} - \mathbf{r}') \mu(\mathbf{r}') \, \mathrm{d}s(\mathbf{r}'). \tag{39}$$

A subtle point here is that the kernel $\partial_{\mathbf{n},\mathbf{n}'}^2 G(\mathbf{r} - \mathbf{r}')$ is not an integrable function for $\mathbf{r}' \to \mathbf{r}$. We, therefore, need to treat p as a distribution, defined through scalar products with suitable test functions. This is unlike $[p]$ which is continuous on $\partial\Omega$.

Given these definitions, we can reinterpret (35a) as showing that a function u harmonic in $\Omega \cup \Omega^c$ is represented as the sum of a single-layer potential [6], [7] corresponding to $\xi = [p]$ and a double-layer potential corresponding to $\mu = -[u]$.

The equations concerning p are summarized in Theorem 3 below, which extends Theorem 2 to the directional and normal derivatives of u.

Theorem 3 (Representation Theorem for p): Let $\Omega \subseteq \mathbb{R}^3$ be a bounded open set with a regular boundary $\partial\Omega$. Let $u : (\Omega \cup \Omega^c) \to \mathbb{R}$ be a function harmonic ($\Delta u = 0$) in both Ω and Ω^c, satisfying condition $\mathcal{H}$. Let also $\mathbf{n}$ (respectively, $\mathbf{n}'$) be the unit normal to $\partial\Omega$ at point $\mathbf{r}$ (respectively, $\mathbf{r}'$) and $\mathbf{m}$ an arbitrary unit vector at $\mathbf{r}$. Then for $\mathbf{r} \notin \partial\Omega$ the following representation holds:

$$p_{\mathbf{m}}(\mathbf{r})$$
$$= \int_{\partial\Omega} -\partial_{\mathbf{m},\mathbf{n}'}^2 G(\mathbf{r}-\mathbf{r}')[u]_{\partial\Omega}(\mathbf{r}') + \partial_{\mathbf{m}} G(\mathbf{r}-\mathbf{r}')[p]_{\partial\Omega}(\mathbf{r}') \mathrm{d}s(\mathbf{r}') \tag{40a}$$

and for $\mathbf{r} \in \partial\Omega$

$$p^{\pm}(\mathbf{r}) \stackrel{\mathrm{def}}{=} p_{\mathbf{n}}^{\pm}(\mathbf{r}) = \mp \frac{[p]_{\partial\Omega}}{2}$$
$$+ \int_{\partial\Omega} -\partial_{\mathbf{n},\mathbf{n}'}^2 G(\mathbf{r}-\mathbf{r}')[u]_{\partial\Omega}(\mathbf{r}') + \partial_{\mathbf{n}} G(\mathbf{r}-\mathbf{r}')[p]_{\partial\Omega}(\mathbf{r}') \mathrm{d}s(\mathbf{r}'). \tag{40b}$$

Analogously to u, the derivative $p = p_{\mathbf{n}}$ given by (40a) for $\mathbf{m} = \mathbf{n}$ converges to $p = (p^+ + p^-)/2$ on $\partial\Omega$ in the distributional sense.

B. Multiple Interfaces

Having in view the layered model depicted in Fig. 1, we extend Theorem 2 to a nested domain topology. As we have seen in Section III-G, it suffices to consider the case of three nested domains as in Fig. 2.

Proposition 1: Let $\Omega_1, \Omega_2, \Omega_3$ be disjoint open sets such that $\overline{\Omega}_1 \cup \overline{\Omega}_2 \cup \overline{\Omega}_3 = \mathbb{R}^3$, separated by regular boundaries $\partial\Omega_1 \cap \partial\Omega_2 = S_1$, $\partial\Omega_2 \cap \partial\Omega_3 = S_2$, and $\partial\Omega_1 \cap \partial\Omega_3 = \emptyset$. Let $u : (\Omega_1 \cup \Omega_2 \cup \Omega_3) \to \mathbb{R}$ be harmonic and satisfy $\mathcal{H}$. Then (35a) and (35b) hold with $\partial\Omega = S_1 \cup S_2$.

Proof: To prove this proposition, we use the third Green identities (32) in Ω_1 and (34) in Ω_3, and the variant (33) in Ω_2. We assume that the normal vector fields $\mathbf{n}_1$ on S_1 and $\mathbf{n}_2$ on S_2 point globally outward (as in Fig. 2). We have

$$\chi_{\Omega_1} u = \mathcal{P}_{S_1,\mathbf{n}_1}^-(u)$$
$$\chi_{\Omega_2} u = -\mathcal{P}_{S_1,\mathbf{n}_1}^+(u) + \mathcal{P}_{S_2,\mathbf{n}_2}^-(u)$$
$$\chi_{\Omega_3} u = -\mathcal{P}_{S_2,\mathbf{n}_2}^+(u).$$

Summing up the three contributions gives

$$\chi_{\Omega_1} u + \chi_{\Omega_2} u + \chi_{\Omega_3} u = \left(\mathcal{P}_{S_1,\mathbf{n}_1}^-(u) - \mathcal{P}_{S_1,\mathbf{n}_1}^+(u) \right)$$
$$+ \left(\mathcal{P}_{S_2,\mathbf{n}_2}^-(u) - \mathcal{P}_{S_2,\mathbf{n}_2}^+(u) \right).$$

For $\mathbf{r} \in \Omega_1 \cup \Omega_2 \cup \Omega_3$, $\chi_{\Omega_1} u(\mathbf{r}) + \chi_{\Omega_2} u(\mathbf{r}) + \chi_{\Omega_3} u(\mathbf{r}) = u(\mathbf{r})$, and we obtain (35a). For $\mathbf{r} \in S_1 \cup S_2$, $\chi_{\Omega_1} u(\mathbf{r}) + \chi_{\Omega_2} u(\mathbf{r}) + \chi_{\Omega_3} u(\mathbf{r}) = (u^+(\mathbf{r}) + u^-(\mathbf{r}))/2$. Since $u^+ = -(1/2)[u]_{\partial\Omega} + (u^+ + u^-)/2$ and $u^- = (1/2)[u]_{\partial\Omega} + (u^+ + u^-)/2$, we obtain (35b). ∎

Theorem 3 also holds in the case of a nested volume topology, but we do not provide the detailed proof here.

The single and double potentials can also easily be applied in the case of our layered model from Fig. 1. For the single-layer potential, we write

$$u_s(\mathbf{r}) = \sum_{i=1}^{N} \int_{S_i} G(\mathbf{r} - \mathbf{r}') \xi_{S_i}(\mathbf{r}') \mathrm{d}s(\mathbf{r}') \tag{41}$$

where each ξ_{S_i} is defined on the corresponding surface S_i. The properties from the single interface case are trivially satisfied thanks to additivity, namely $[u_s]_i = 0$ and $[\partial_{\mathbf{n}} u_s]_i = \xi_i$. More specifically

$$p_{\mathbf{n}}^{\pm}(\mathbf{r}) = \partial_{\mathbf{n}} u_s^{\pm}(\mathbf{r})$$
$$= \mp \frac{\xi_{S_j}(\mathbf{r})}{2} + \sum_{i=1}^{N} \int_{S_i} \partial_{\mathbf{n}} G(\mathbf{r} - \mathbf{r}') \xi_{S_i}(\mathbf{r}') \mathrm{d}s(\mathbf{r}')$$

for $\mathbf{r} \in S_j$. Similarly, for the double-layer potential, we have

$$u_d(\mathbf{r}) = \sum_{i=1}^{N-1} \int_{S_i} \partial_{\mathbf{n}'} G(\mathbf{r} - \mathbf{r}') \mu_{S_i}(\mathbf{r}') \mathrm{d}s(\mathbf{r}') \tag{42}$$

with $[u_d]_i = -\mu_{S_i}$, $[\partial_{\mathbf{n}} u_d] = 0$ and

$$u_d^{\pm}(\mathbf{r}) = \pm \frac{\mu_{S_j}(\mathbf{r})}{2} + \sum_{i=1}^{N} \int_{S_i} \partial_{\mathbf{n}'} G(\mathbf{r} - \mathbf{r}') \mu_{S_i}(\mathbf{r}') \, \mathrm{d}s(\mathbf{r}') \tag{43}$$

for $\mathbf{r} \in S_j$.

C. Uniqueness

The integral representation in terms of $\mu = -[u]$ and $\xi = [p]$ is unique, if u and p are considered as a pair [7]. In other words, there is only one pair of (μ, ξ) generating a given set

of pairs (u^-, p^-), (u^+, p^+), or $([u], [p])$. However, this is no longer true if only p^- is given (interior Neumann problem), as any constant function can be added to u. Physically, this means that the potential is only known up to a constant. To get rid of this indetermination, we can for example choose to impose $\langle u, 1 \rangle = 0$; other options are possible [33]. In the same spirit, note that for harmonic u, Stokes' theorem necessarily imposes $\langle p, 1 \rangle = 0$ on any closed surface.

D. Weak Regularity

We need to extend Theorems 2 and 3 to nonregular surfaces,[13] such as for example a triangulated surface which is not regular on the edges and at the vertices. We find that the equations in Theorems 2 and 3 hold, provided that there are not "too many" singular points (their set is of zero measure) and that we only evaluate the integrals in (35b) and (40b) at the regular points. If needed, the values/limits on the surface can still be calculated even at the singular points by a more complex expression involving inner and outer spherical angles [10], [43]. We will avoid this complication here by concentrating on the Galerkin method that gives better results and does not require pointwise values.

In a similar vein, we can relax the continuity requirements on $\mu = -[u]$, $\xi = [p]$, in order to approximate them by some $\tilde{\mu}, \tilde{\xi}$. Only piecewise continuity is necessary for the convergence of the integrals in Theorems 2 and 3 (again with a zero measure set of discontinuity points) if we do not evaluate (35b) and (40b) at the points of discontinuity.

REFERENCES

[1] J. Phillips, R. Leahy, J. Mosher, and B. Timsari, "Imaging neural activity using MEG and EEG," *IEEE Eng. Med. Biol. Mag.*, vol. 16, no. 3, pp. 34–42, May-Jun. 1997.

[2] J. Sarvas, "Basic mathematical and electromagnetic concepts of the biomagnetic inverse problem," *Phys. Med. Biol.*, vol. 32, no. 1, pp. 11–22, 1987.

[3] M. Hämäläinen, R. Hari, R. J. IImoniemi, J. Knuutila, and O. V. Lounasmaa, "Magnetoencephalography—Theory, instrumentation, and applications to noninvasive studies of the working human brain," *Rev. Mod. Phys.*, vol. 65, no. 2, pp. 413–497, Apr. 1993.

[4] D. B. Geselowitz, "On the magnetic field generated outside an inhomogeneous volume conductor by internal volume currents," *IEEE Trans. Magn.*, vol. MAG-6, pp. 346–347, 1970.

[5] O. Faugeras, F. Clément, R. Deriche, R. Keriven, T. Papadopoulo, J. Roberts, T. Viéville, F. Devernay, J. Gomes, G. Hermosillo, P. Kornprobst, and D. Lingrand, "The Inverse EEG and MEG Problems: The Adjoint Space Approach I: The Continuous Case," INRIA, Sophia Antipolis, France, Tech. Rep. 3673, 1999.

[6] M. Bonnet, *Equations Intégrales et Éléments de Frontière*, CNRS ed. Eyrolles, France: Eyrolles, 1995.

[7] J.-C Nédélec, *Acoustic and Electromagnetic Equations*. Berlin, Germany: Springer-Verlag, 2001.

[8] J. Rahola and S. Tissari, "Iterative solution of dense linear systems arising from the electrostatic integral equation," *Phys. Med. Biol.*, no. 47, pp. 961–975, 2002.

[9] ——, "Iterative Solution of Dense Linear Systems Arising From Boundary Element Formulations of the Biomagnetic Inverse Problem," CERFACS, Toulouse, France, Tech. Rep. TR/PA/98/40, 1998.

[10] A. S. Ferguson and G. Stroink, "Factors affecting the accuracy of the boundary element method in the forward problem—I: Calculating surface potentials," *IEEE Trans. Biomed. Eng.*, vol. 44, no. 11, pp. 1139–1155, Nov. 1997.

[11] M. Clerc, R. Keriven, O. Faugeras, J. Kybic, and T. Papadopoulo, "The fast multipole method for the direct E/MEG problem," presented at the ISBI, Washington, D.C., July 2002.

[12] S. Tissari and J. Rahola, "Error Analysis of a New Galerkin Method to Solve the Forward Problem in MEG and EEG Using the Boundary Element Method," CERFACS, Toulouse, France, Tech. Rep. TR/PA/98/39, 1998.

[13] M. S. Hämäläinen and J. Sarvas, "Realistic conductivity geometry model of the human head for interpretation of neuromagnetic data," *IEEE Trans. Biomed. Eng.*, vol. 36, no. 2, pp. 165–171, Feb. 1989.

[14] S. Tissari and J. Rahola, "A precorrected-FFT method to accelerate the solution of the forward problem in MEG," *Phys. Med. Biol.*, vol. 48, pp. 523–541, 2003.

[15] Z. Zhang and D. L. Jewett, "Insidious errors in dipole localization parameters at a single time-point due to model misspecification of number of shells," *Electroencephalogr. Clin. Neurophysiol.*, no. 88, pp. 1–11, 1993.

[16] R. Leahy, J. Mosher, M. Spencer, M. Huang, and J. Lewine, "A Study of Dipole Localization Accuracy for MEG and EEG Using a Human Skull Phantom," Los Alamos National Laboratory, Los Alamos, NM, Tech Rep LA-UR-98-1442, 1998.

[17] D. B. Geselowitz, "On bioelectric potentials in an homogeneous volume conductor," *Biophys. J.*, vol. 7, pp. 1–11, 1967.

[18] F. Babiloni, C. Del Gratta, F. Carducci, C. Babiloni, G. M. Roberti, V. Pizzella, P. M. Rossini, G. L. Romani, and A. Urbano, "Combined high resolution EEG and MEG data for linear inverse estimate of human event-related cortical activity," in *Proc. 20th Annu. Int. Conf. IEEE Eng. Med. Biol. Soc.*, 1998, pp. 2151–2154.

[19] J. C. de Munck, "A linear discretization of the volume conductor boundary integral equation using analytically integrated elements," *IEEE Trans. Biomed. Eng.*, vol. 39, no. 9, pp. 986–990, Sept. 1992.

[20] J. C. Mosher, R. B. Leahy, and P. S. Lewis, "EEG and MEG: Forward solutions for inverse methods," *IEEE IEEE Trans. Biomed. Eng.*, vol. 46, no. 3, pp. 245–259, Mar. 1999.

[21] J. C. Mosher, R. M. Leahy, and P. S. Lewis, "Matrix Kernels for the Forward Problem in EEG and MEG," Los Alamos Nat. Lab., Los Alamos, NM, Tech. Rep. LA-UR-97-3812, 1997.

[22] N. G. Gençer and I. O. Tanzer, "Forward problem solution of electromagnetic source imaging using a new BEM formulation with high-order elements," *Phys. Med. Biol.*, vol. 44, no. 9, pp. 2275–2287, 1999.

[23] L. J. Gray and G. H. Paulino, "Symmetric Galerkin boundary integral formulation for interface and multi-zone problems," *Int. J. Numer. Methods Eng.*, vol. 40, no. 16, pp. 3085–3103, 1997.

[24] J. B. Layton, S. Ganguly, C. Balakrishna, and J. H. Kane, "A symmetric Galerkin multi-zone boundary element formulation," *Int. J. Numer. Methods Eng.*, vol. 40, no. 16, pp. 2913–2931, 1997.

[25] S. H. Christiansen, "Résolution des Équations Intégrales Pour la Diffraction D'Ondes Acoustiques et Électromagnétiques," Ph.D. dissertation, Ecole Polytechnique, 2002.

[26] R. Dautray and J.-L. Lions, *Mathematical Analysis and Numerical Methods for Science and Technology*. Berlin, Germany: Springer-Verlag, 2000, vol. 6.

[27] J. Lötjönen, "Construction of Boundary Element Models in Bioelectromagnetism," Ph.D., Helsinki University of Technology, Espoo, Finland, 2000.

[28] D. Van't Ent, J. C. De Munck, and A. L. Kaas, "A fast method to derive realistic BEM models for E/MEG source reconstruction," *IEEE Trans. Biomed. Eng.*, vol. 48, Dec. 2001.

[29] D. R. Wilton, S. M. Rao, A. W. Glisson, D. H. Schaubert, O. M. Al-Bundak, and C. M. Butler, "Potential integrals for uniform and linear source distributions on polygonal and polyhedral domains," *IEEE Trans. Antennas Propag.*, vol. 32, no. AP–3, pp. 276–281, Mar. 1984.

[30] A. S. Ferguson, X. Zhang, and G. Stroink, "A complete linear discretization for calculating the magnetic field using the boundary element method," *IEEE Trans. Biomed. Eng.*, vol. 41, no. 5, pp. 455–459, May 1994.

[31] J. N. Lyness and D. Jespersen, "Moderate degree symmetric quadrature rules for the triangle," *J. Inst. Math Applicat.*, vol. 15, pp. 19–32, 1975.

[32] T. F. Chan, "Deflated decomposition solution of nearly singular systems," *SIAM J. Numer. Anal.*, vol. 21, pp. 739–754, 1984.

[33] G. Fischer, B. Tilg, R. Modre, F. Hanser, B. Messnarz, and P. Wach, "On modeling the Wilson terminal in the boundary and finite element method," *IEEE Trans. Biomed. Eng.*, vol. 49, no. 3, pp. 217–224, Mar. 2002.

[34] G. Strang and G. Fix, "A Fourier analysis of the finite element variational method," in *Constructive Aspect of Functional Analysis*. Rome, Italy: Cremonese, 1971, pp. 796–830.

---

[13]A surface is regular if it can be locally approximated by a linear function everywhere.

[35] R. Barret, M. Berry, T. F. Chan, J. Demmel, J. Donato, J. Dongarra, V. Eijkhout, R. Pozo, C. Romine, and H. van der Vonst, *Templates for the Solution of Linear Systems: Building Blocks for Iterative Methods*. Philadelphia: SIAM, 1994.

[36] J. R. Phillips and J. K. White, "A precorrected-FFT method for electrostatic analysis of complicated 3-D structures," *IEEE Trans. Computer-Aided Design Integr. Circuits Syst.*, vol. 16, no. 10, Oct. 1997.

[37] J. C. De Munck, "The potential distribution in a layered anisotropic spheroidal volume conductor," *J. Appl. Phys*, vol. 2, no. 64, pp. 464–470, July 1988.

[38] Z. Zhang, "A fast method to compute surface potentials generated by dipoles within multilayer anisotropic spheres," *Phys. Med. Biol.*, vol. 40, pp. 335–349, 1995.

[39] U. Schmitt, A. K. Louis, F. Darvas, H. Buchner, and M. Fuchs, "Numerical aspects of spatio-temporal current density reconstruction from EEG/MEG-data," *IEEE Trans. Med. Imag.*, vol. 20, no. 4, pp. 314–324, Apr. 2001.

[40] R. Van Uitert and C. Johnson, "Can a spherical model substitute for a realistic head model in forward and inverse MEG simulations?," in *Proc. BIOMAG*, 2002, pp. 798–800.

[41] J. Kybic and M. Clerc, "Symmetric BEM and multiscale fast multipole method for the E/MEG problem," presented at the 4th Int. Symp. Non-invasive Functional Source Imaging Within the Human Brain and Heart, Chieti, Italy, Sept. 2003.

[42] L. Evans, "Partial differential equations," in *Proc. Am. Math. Soc.*, vol. 19, Graduate Studies in Mathematics, 1998.

[43] J. W. H. Meijs, O. W. Weier, M. J. Peters, and A. van Oosterom, "On the numerical accuracy of the boundary element method," *IEEE Trans. Biomed. Eng.*, vol. 36, no. 10, pp. 1038–1049, Oct. 1989.